

Proper Orthogonal Decomposition Closure Models For Turbulent Flows: A Numerical Comparison

Zhu Wang¹, Imran Akhtar², Jeff Borggaard¹, and Traian Iliescu¹

¹Department of Mathematics, Virginia Tech, Blacksburg, VA 24061-0123, U.S.A.

²Department of Mechanical Engineering, NUST College of Electrical & Mechanical Engineering, National University of Sciences & Technology, Islamabad, Pakistan.

(Received 26 November 2024 and in revised form ??)

This paper puts forth two new closure models for the proper orthogonal decomposition reduced-order modeling of structurally dominated turbulent flows: the dynamic subgrid-scale model and the variational multiscale model. These models, which are considered state-of-the-art in large eddy simulation, together with the mixing length and the Smagorinsky closure models, are tested in the numerical simulation of a 3D turbulent flow around a circular cylinder at $Re = 1,000$. Two criteria are used in judging the performance of the proper orthogonal decomposition reduced-order models: the kinetic energy spectrum and the time evolution of the POD coefficients. All the numerical results are benchmarked against a direct numerical simulation. Based on these numerical results, we conclude that the dynamic subgrid-scale and the variational multiscale models perform best.

Key Words: Proper orthogonal decomposition, reduced-order modeling, turbulence, large eddy simulation, eddy viscosity, variational multiscale, dynamic subgrid-scale model.

1. Introduction

Reduced-order models (ROMs) of structurally dominated turbulent flows are central to many applications in science and engineering, such as fluid flow control (see for example Ito & Ravindran 1998; Graham *et al.* 1999; Cohen *et al.* 2003; Bergmann *et al.* 2005; Lehmann *et al.* 2005; Hoepffner *et al.* 2006; Bagheri *et al.* 2009; Barbagallo *et al.* 2009; Ahuja & Rowley 2010; Akhtar & Nayfeh 2010) and data assimilation of atmospheric and oceanic flows (Luo *et al.* 2007; Daescu & Navon 2008; Fang *et al.* 2009). Both computational efficiency and physical accuracy are needed for the success of these ROMs in practical applications. Striking a balance between efficiency and accuracy in ROMs of turbulent flows is, of course, challenging. Indeed, it is clear that the fewer the modes retained in the ROM, the more efficient the ROM is. Preserving the physical accuracy of the resulting ROM, however, becomes challenging, since the modes that are not retained in the ROM representation of the underlying turbulent flow need to be modeled. The quest of balancing the computational efficiency and physical accuracy represents one of the main challenges in ROMs for turbulent flows.

One of the most successful ROM strategies for structurally dominated turbulent flows has been the *Proper Orthogonal Decomposition (POD)* (see for example Holmes *et al.* 1996; Sirovich 1987). POD starts with data from an accurate numerical simulation (or

physical experiment), extracts the most energetic modes in the system, and utilizes a Galerkin procedure that yields a ROM of the underlying turbulent flow. The first *proper orthogonal decomposition reduced-order model (POD-ROM)* for the turbulent boundary layer was proposed in Aubry *et al.* (1988). This model truncated the POD basis and used an eddy viscosity-based approximation to model the effect of the discarded POD modes on the POD modes kept in the model. This POD-ROM yielded good qualitative results, considering the coarseness of the approximation. The criterion used to assess the accuracy of the model was the intermittency of bursting events in the turbulent boundary layer. This POD-ROM was further investigated numerically in two subsequent papers (Podvin & Lumley 1998; Podvin 2001). The model reproduced the qualitative physics of the turbulent boundary layer well. Furthermore, by adding new POD modes to the model, the accuracy of the model was increased.

Despite their initial success, POD-ROMs have generally been limited to laminar flows and relatively few reports on closure modeling strategies for turbulent flows have appeared in the literature (Aubry *et al.* 1988; Podvin & Lumley 1998; Podvin 2001; Rempfer & Fasel 1994; Rempfer 1996; Cazemier *et al.* 1998; Ma & Karniadakis 2002; Sirisup & Karniadakis 2004; Buffoni *et al.* 2006; Noack *et al.* 2002, 2003, 2005, 2008; Ullmann & Lang 2010; Hay *et al.* 2009, 2010). This is in stark contrast to the amount of work done in traditional turbulence modeling, such as *large eddy simulation (LES)*, where literally hundreds of closure models have been proposed and investigated (see for example Sagaut 2006) over the same time period. This disparity in closure modeling between POD reduced-order modeling and classical turbulence modeling seems even more dramatic considering that the concept of an energy cascade, which is a fundamental modeling principle in LES, is also valid in a POD setting. Indeed, the validity of the extension of the energy cascade concept to the POD setting was investigated numerically in Couplet *et al.* (2003). The authors have investigated the energy transfer among POD modes in a non-homogeneous computational setting. By monitoring the triad interactions due to the nonlinear term in the Navier-Stokes equations, they have concluded that the transfer of energy among the POD modes is similar to the transfer of energy among Fourier modes. Specifically, they found that there is a net forward energy transfer from low index POD modes to higher index POD modes and that this transfer of energy is local in nature (that is, energy is mainly transferred among POD modes whose indices are close to one another). This study (see also Noack *et al.* 2002) clearly suggests that LES ideas based on the energy cascade concept could also be used in devising POD-ROMs.

One of the main reasons for the scarcity of closure models for POD-ROMs of turbulent flows is the impractical cost of standard LES closure models employed in a POD-ROM setting. Indeed, most of the computational cost of a POD-ROM lies in assembling the vectors, matrices and tensors of the ROM. This, however, is hardly a problem for POD-ROM, since the vectors, matrices and tensors are assembled only *once*, at the beginning of the POD-ROM simulation, and reused at every time step. Standard (nonlinear) LES closure models, however, introduce new vectors and matrices that need to be recomputed at every time step. Thus, a straightforward numerical discretization of such closure models would come at a huge computational cost, rendering the resulting POD-ROMs impractical.

In the past few years, a number of strategies have been introduced to treat nonlinear terms in POD-ROMs. These include interpolatory methods such as the empirical interpolation method (Barrault *et al.* 2004; Chaturantabut *et al.* 2010; Galbally *et al.* 2010), the closely related group finite element approach (Dickinson & Singler 2010) and a novel two-level discretization method (Wang *et al.* 2011). The latter approach is best suited for this study since it does not constrain the nonlinear term to lie within a predefined set.

This approach is based on a two-level discretization of the vectors, matrices and tensors of the POD-ROM, in which all the terms are computed on the fine grid, except for the nonlinear closure model terms, which are computed on a coarser grid. In Wang *et al.* (2011), numerical simulations of a turbulent flow past a 3D cylinder at $Re = 1,000$ with a standard LES closure model (Smagorinsky 1963) have shown that the new two-level discretization is both computationally efficient and physically accurate. Indeed, the new two-level algorithm decreased by more than an order of magnitude the CPU time of the standard one-level algorithm, without compromising the physical accuracy.

In this report, we use the two-level algorithm proposed in Wang *et al.* (2011) to discretize two new POD-ROMs, inspired from state-of-the-art LES closure modeling strategies: the *dynamic subgrid-scale (DS) model* (Germano *et al.* 1991; Meneveau *et al.* 1996; Porté-Agel *et al.* 2000) and the *variational multiscale (VMS) model* (Hughes *et al.* 2000). We also consider the standard mixing-length closure model proposed in Aubry *et al.* (1988) and the Smagorinsky model proposed in Wang *et al.* (2011) (see also Noack *et al.* 2002; Ullmann & Lang 2010), both being standard LES closure models. All four POD-ROMs are tested in the numerical simulation of a 3D turbulent flow around a circular cylinder at $Re = 1,000$. Two criteria are used in judging the performance of the POD-ROMs: the kinetic energy spectrum and the time evolution of the POD coefficients. All the numerical results are benchmarked against a direct numerical simulation.

The rest of the paper is organized as follows: The general methodology used in the development of POD-ROMs is presented in § 2. The four POD closure models are described in § 3 and are investigated numerically in § 4. Finally, conclusions and several research directions currently pursued by our group are provided in § 5.

2. POD Reduced-Order Modeling

We now present the general approach used in the development of POD-ROMs. We start by briefly describing the POD methodology. For more details, the reader is referred to Sirovich (1987); Holmes *et al.* (1996). To this end, we consider the numerical solution of the incompressible *Navier-Stokes equations (NSE)*:

$$\left. \begin{aligned} \mathbf{u}_t - \text{Re}^{-1} \Delta \mathbf{u} + (\mathbf{u} \cdot \nabla) \mathbf{u} + \nabla p &= 0 \\ \nabla \cdot \mathbf{u} &= 0, \end{aligned} \right\} \quad (2.1)$$

where \mathbf{u} is the velocity, p the pressure and Re the Reynolds number. The POD basis is generated by post-processing typical data from the numerical simulation of (2.1). If $\mathcal{Y} = \{\mathbf{y}(\cdot, t) \in \mathcal{H} \mid t \in (0, T)\}$ (with \mathcal{H} a Hilbert space) represents a simulation of the NSE, then the first POD basis vector is the function that maximizes the time-averaged projection of \mathcal{Y} onto itself,

$$\varphi_1 = \max_{\varphi \in \mathcal{H}, \|\varphi\|_{\mathcal{H}}=1} \frac{1}{T} \int_0^T |\langle \mathbf{y}(\cdot, t), \varphi(\cdot) \rangle_{\mathcal{H}}|^2 dt. \quad (2.2)$$

Subsequent vectors, φ_k , are determined by seeking the above maximum in the orthogonal complement to

$$\mathbf{X}^{k-1} = \text{span}\{\varphi_1, \dots, \varphi_{k-1}\}, \quad 2 \leq k \leq N, \quad \text{in } \mathcal{H}, \quad (2.3)$$

where N is the rank of \mathcal{Y} . If we choose $\mathcal{H} = \mathcal{L}_2$ and \mathcal{Y} represents a single simulation, the POD basis functions satisfy the Fredholm integral equation

$$\int_{\Omega} \mathbf{R}(\mathbf{x}, \mathbf{x}') \varphi_i(\mathbf{x}') d\mathbf{x}' = \lambda_i \varphi_i(\mathbf{x}), \quad (2.4)$$

where

$$\mathbf{R}(\mathbf{x}, \mathbf{x}') = \frac{1}{T} \int_0^T \mathbf{y}(\mathbf{x}, t) \mathbf{y}^*(\mathbf{x}', t) dt \quad (2.5)$$

is the spatial autocorrelation kernel. There are natural extensions of this definition that accommodate multiple simulations. In practice, either the time average of each simulation or the steady state solution is removed, so that \mathcal{Y} contains fluctuation from the mean (or a centering trajectory), e.g., $\mathbf{y}(\mathbf{x}, t) = \mathbf{u}(\mathbf{x}, t) - \mathbf{U}(\mathbf{x})$ (Holmes *et al.* 1996). Note that each POD basis vector $\boldsymbol{\varphi}_k$ represents a weighted time average of the data \mathcal{Y} . Thus, these basis vectors preserve linear properties (such as the divergence-free property).

A POD basis enables a reduced representation of the simulated data, and thus can be viewed as a compression algorithm. Utilizing the POD basis to obtain efficient approximations to (2.1) is achieved using the POD basis in a Galerkin approximation, and employing the fact that the POD basis vectors are mutually orthogonal. A POD-ROM of the flow is constructed from the POD basis by writing

$$\mathbf{u}(\mathbf{x}, t) \approx \mathbf{u}_r(\mathbf{x}, t) \equiv \mathbf{U}(\mathbf{x}) + \sum_{j=1}^r a_j(t) \boldsymbol{\varphi}_j(\mathbf{x}), \quad (2.6)$$

where $\mathbf{U}(\mathbf{x})$ is the centering trajectory, $\{\boldsymbol{\varphi}_j\}_{j=1}^r$ are the first r POD basis vectors, and $\{a_j(t)\}_{j=1}^r$ are the sought time-varying coefficients that represent the POD-Galerkin trajectories. We now replace the velocity \mathbf{u} with \mathbf{u}_r in the NSE (2.1), and then project the resulting equations onto the subspace \mathbf{X}^r . Using the boundary conditions and the fact that all modes are solenoidal, one obtains the *POD Galerkin reduced-order model (POD-G-ROM)*:

$$\left(\frac{\partial \mathbf{u}_r}{\partial t}, \boldsymbol{\varphi} \right) + ((\mathbf{u}_r \cdot \nabla) \mathbf{u}_r, \boldsymbol{\varphi}) + \left(\frac{2}{Re} \mathbb{D}(\mathbf{u}_r), \nabla \boldsymbol{\varphi} \right) = 0 \quad \forall \boldsymbol{\varphi} \in \mathbf{X}^r, \quad (2.7)$$

where $\mathbb{D}(\mathbf{u}_r) := (\nabla \mathbf{u}_r + (\nabla \mathbf{u}_r)^T)/2$ is the deformation tensor of \mathbf{u}_r . We note that, since the computational domain that we consider is large enough, the pressure terms in (2.7) can be neglected (for details, see Noack *et al.* 2005; Akhtar *et al.* 2009). The POD-G-ROM (2.7) yields the following autonomous dynamical system for the vector of time coefficients, $\mathbf{a}(t)$:

$$\dot{\mathbf{a}} = \mathbf{b} + \mathbf{A}\mathbf{a} + \mathbf{a}^T \mathbf{B}\mathbf{a}, \quad (2.8)$$

where \mathbf{b} , \mathbf{A} , and \mathbf{B} correspond to the constant, linear, and quadratic terms in the numerical discretization of the NSE (2.1), respectively. The initial conditions are obtained by projection:

$$a_j(0) = \langle \boldsymbol{\varphi}_j, \mathbf{u}(\cdot, 0) - \mathbf{U}(\cdot) \rangle_{\mathcal{H}}, \quad j = 1, \dots, r. \quad (2.9)$$

The finite dimensional system (2.8) can be written componentwise as follows: For all $k = 1, \dots, r$,

$$\dot{a}_k(t) = b_k + \sum_{m=1}^r A_{km} a_m(t) + \sum_{m=1}^r \sum_{n=1}^r B_{kmn} a_n(t) a_m(t), \quad (2.10)$$

where

$$b_k = -(\varphi_k, \mathbf{U} \cdot \nabla \mathbf{U}) - \frac{2}{\text{Re}} \left(\nabla \varphi_k, \frac{\nabla \mathbf{U} + \nabla \mathbf{U}^T}{2} \right), \quad (2.11)$$

$$A_{km} = -(\varphi_k, \mathbf{U} \cdot \nabla \varphi_m) - (\varphi_k, \varphi_m \cdot \nabla \mathbf{U}) - \frac{2}{\text{Re}} \left(\nabla \varphi_k, \frac{\nabla \varphi_m + \nabla \varphi_m^T}{2} \right), \quad (2.12)$$

$$B_{kmn} = -(\varphi_k, \varphi_m \cdot \nabla \varphi_n). \quad (2.13)$$

3. POD Closure Models

In this section, we present the four POD closure models investigated numerically in §4. To this end, we start by describing the filtering operation utilized and the spatial length-scale δ used in the POD closure models. Both are needed in order to define meaningful LES-inspired POD closure models.

3.1. POD Filter

In LES, the filter is the central tool used to obtain simplified mathematical models that are computationally tractable. The filtering operation is effected by convolution of flow variables with a rapidly decaying *spatial* filter g_δ , where δ is the radius of the spatial filter. In POD, however, there is no explicit spatial filter used. Thus, in order to develop LES-type POD closure models, a POD filter needs to be introduced. Given the hierarchical nature of the POD basis, a natural such filter appears to be the Galerkin projection. For all $\mathbf{u} \in \mathbf{X}$, the Galerkin projection $\bar{\mathbf{u}} \in \mathbf{X}^r$ is the solution of the following equation:

$$(\mathbf{u} - \bar{\mathbf{u}}, \varphi) = 0 \quad \forall \varphi \in \mathbf{X}^r. \quad (3.1)$$

The Galerkin projection defined in (3.1) will be the filter used in all POD closure models studied in this report.

3.2. POD Lengthscale

Next, we introduce the lengthscale δ used in the POD closure models. We emphasize that this choice is one of the fundamental issues in making a connection with LES. Indeed, we need such a lengthscale (δ) in order to define dimensionally sound POD models of LES flavor.

To derive the lengthscale δ , we use dimensional analysis. Aubry *et al.* (1988) defined $l_>$, a dimensionally sound lengthscale for a turbulent pipe flow. In fact, this lengthscale was only defined implicitly, through the turbulent eddy viscosity $\nu_T := u_> l_>$. Indeed, equation (22) in Aubry *et al.* (1988) reads

$$\nu_T := u_> l_> = \frac{\int_0^{X_2} \langle u_{i>} u_{i>} \rangle dx_2}{\left(X_2 \int_0^{X_2} \langle u_{i>,j} u_{i>,j} \rangle dx_2 \right)^{1/2}}, \quad (3.2)$$

where repeated indices denote summation, the subscript $>$ denotes unresolved POD modes,

$$\langle f \rangle = \frac{1}{L_1 L_3} \int_0^{L_1} \int_0^{L_3} f(\mathbf{x}, t) dx_1 dx_3 \quad (3.3)$$

denotes the spatial average of f in the homogeneous directions (here x_1 and x_3), and L_1, L_3 and X_2 are the streamwise, spanwise, and wall-normal dimensions of the computational domain, respectively. Note that the authors only considered the wall region, not the

entire pipe flow. In (3.2), the following notation was used: $u_{i>} = \sum_{j=r+1}^N a_j^i \varphi_j$, $u_{i>} u_{i>} = \sum_{i=1}^3 u_{i>} u_{i>}$, and $u_{i>,j} = \frac{\partial u_{i>}}{\partial x_j}$. Note that a quick dimensional analysis shows that the quantity defined in (3.2) has the dimensions of a viscosity. Indeed,

$$[\nu_T] = \frac{\frac{m}{s} \frac{m}{s} m}{[m (\frac{1}{s} \frac{1}{s} m)]^{1/2}} = \frac{\frac{m^3}{s^2}}{\frac{m}{s}} = \frac{m^2}{s}. \quad (3.4)$$

In Appendix B of Aubry *et al.* (1988), the authors have further simplified (3.2) and expressed ν_T in terms of the first neglected POD modes:

$$\nu_T := u_{>} l_{>} = \frac{\sum_{(\mathbf{k},n)} \lambda_{\mathbf{k}}^{(n)}}{\left(X_2 L_1 L_3 \sum_{(\mathbf{k},n)} \lambda_{\mathbf{k}}^{(n)} \left(\int_0^{X_2} D\Phi_{i_{\mathbf{k}}}^{(n)} D\Phi_{i_{\mathbf{k}}}^{(n)*} dx_2 - k_1^2 - k_3^2 \right) \right)^{1/2}}, \quad (3.5)$$

where the triplets (\mathbf{k}, n) are the first neglected POD modes.

In equation (9.90) in Holmes *et al.* (1996), the authors define another dimensionally sound turbulent viscosity

$$\nu_T := u_{>} l_{>} = \frac{1}{X_2} \int_0^{X_2} \frac{\langle u_{i>} u_{i>} \rangle}{\langle u_{i>,j} u_{i>,j} \rangle^{1/2}} dx_2. \quad (3.6)$$

A quick dimensional analysis shows that the quantity defined in (3.6) also has the dimensions of a viscosity.

We can use the two definitions of ν_T in (3.2) and (3.6) to define a lengthscale $l_{>}$. We obtain

$$l_{>} := \frac{\int_0^{X_2} \langle u_{i>} u_{i>} \rangle dx_2}{X_2 \int_0^{X_2} \langle u_{i>,j} u_{i>,j} \rangle dx_2} \quad (3.7)$$

and

$$l_{>} := \left(\frac{1}{X_2} \int_0^{X_2} \frac{\langle u_{i>} u_{i>} \rangle}{\langle u_{i>,j} u_{i>,j} \rangle} dx_2 \right)^{1/2}, \quad (3.8)$$

respectively.

For our 3D flow past a cylinder, both (3.7) and (3.8) are valid candidates for the definition of the lengthscale δ . The only modification we need to make (due to our computational domain) is to replace the horizontal averaging by spanwise averaging and take double integrals in the remaining directions. Specifically, we have

$$\delta := \left(\frac{\int_0^{L_1} \int_0^{L_2} \langle u_{i>} u_{i>} \rangle dx_1 dx_2}{\int_0^{L_1} \int_0^{L_2} \langle u_{i>,j} u_{i>,j} \rangle dx_1 dx_2} \right)^{1/2} \quad (3.9)$$

and

$$\delta := \left(\frac{1}{L_1 L_2} \int_0^{L_1} \int_0^{L_2} \frac{\langle u_{i>} u_{i>} \rangle}{\langle u_{i>,j} u_{i>,j} \rangle} dx_1 dx_2 \right)^{1/2}. \quad (3.10)$$

3.3. POD Closure Models

We are now ready to present the four POD closure models that will be investigated numerically in §4.

The POD-G-ROM (2.7) can be used for laminar flows. For structurally dominated turbulent flows, however, the POD-G-ROM simply fails (Wang *et al.* 2011). The reason is that the effect of the discarded POD modes $\{\varphi_{r+1}, \dots, \varphi_N\}$ needs to be included in the model. For turbulent flows, the most natural way to tackle this *POD closure problem* is by using the *eddy viscosity (EV)* concept. Indeed, most closure models used in turbulence modeling are based on this EV concept, which states that the role of the discarded modes is to extract energy from the system. The concept of energy cascade, which is well established in a Fourier setting, has been recently confirmed in a POD setting in the numerical investigations in Couplet *et al.* (2003). Thus, using LES inspired EV closure models in POD-ROM represents a natural step.

In this section, we propose two new POD closure models: the dynamic subgrid-scale model and the variational multiscale model. We emphasize that, although these models were announced in Borggaard *et al.* (2008), this study represents their *first* careful derivation and thorough numerical investigation. We also numerically test the mixing-length (Aubry *et al.* 1988) and Smagorinsky (Noack *et al.* 2002; Ullmann & Lang 2010; Wang *et al.* 2011) POD closure models.

Since all four POD closure models are of EV type, we first present a general EV POD-ROM framework. Then, for each closure model, we specify the changes that need to be made to this general framework. The general EV POD-ROM framework can be written as:

$$\dot{\mathbf{a}} = \left(\mathbf{b} + \tilde{\mathbf{b}}(\mathbf{a}) \right) + \left(\mathbf{A} + \tilde{\mathbf{A}}(\mathbf{a}) \right) \mathbf{a} + \mathbf{a}^T \mathbf{B} \mathbf{a}, \quad (3.11)$$

which is just a slight modification of the POD-G-ROM (2.8). The new terms in (3.11) (the vector $\tilde{\mathbf{b}}(\mathbf{a})$ and the matrix $\tilde{\mathbf{A}}(\mathbf{a})$) correspond to the numerical discretization of the POD closure model. In componentwise form, equation (3.11) can be written as

$$\begin{aligned} \dot{a}_k(t) = & \left(b_k + \tilde{b}_k(\mathbf{a}) \right) + \sum_{m=1}^r \left(A_{km} + \tilde{A}_{km}(\mathbf{a}) \right) a_m(t) \\ & + \sum_{m=1}^r \sum_{n=1}^r B_{kmn} a_n(t) a_m(t), \end{aligned} \quad (3.12)$$

where b_k , A_{km} , and B_{kmn} are the same as those in equations (2.8) and $\tilde{b}_k(\mathbf{a})$ and $\tilde{A}_{km}(\mathbf{a})$ depend on the specific closure model used.

3.3.1. The mixing-length POD reduced-order model (ML-POD-ROM)

The first POD closure model was the *mixing-length* model proposed in Aubry *et al.* (1988). This closure model is of EV type and amounts to increasing the viscosity coefficient ν by

$$\nu_{ML} = \alpha \nu_T = \alpha U_{ML} L_{ML}, \quad (3.13)$$

where U_{ML} and L_{ML} are characteristic velocity and length scales for the unresolved scales, and α is an $\mathcal{O}(1)$ nondimensional parameter that characterizes the energy being dissipated. Using the EV ansatz in (3.13), the *mixing-length POD reduced-order model*

(ML-POD-ROM) has the form in (3.11), where

$$\tilde{b}_k(\mathbf{a}) = -\nu_{ML} \left(\nabla \varphi_k, \frac{\nabla \mathbf{U} + \nabla \mathbf{U}^T}{2} \right), \quad (3.14)$$

$$\tilde{A}_{km}(\mathbf{a}) = -\nu_{ML} \left(\nabla \varphi_k, \frac{\nabla \varphi_m + \nabla \varphi_m^T}{2} \right). \quad (3.15)$$

The parameter α is expected to vary in a real turbulent flow, and different values of α may result in different dynamics of the flow (Aubry *et al.* 1988; Holmes *et al.* 1996; Podvin & Lumley 1998; Podvin 2001). There are also different ways to define ν_T in (3.11): relation (3.2) was used in Aubry *et al.* (1988), whereas relation (3.6) was used in Holmes *et al.* (1996). We also mention that several other authors have used the ML-POD-ROM (3.13) (see for example Borggaard *et al.* 2008; Wang *et al.* 2011). Improvements to the mixing-length model (3.13) in which the EV coefficient is mode dependent were proposed in Rempfer & Fasel (1994); Cazemier *et al.* (1998); Podvin (2009).

3.3.2. The Smagorinsky POD reduced-order model (S-POD-ROM)

A potential improvement over the simplistic mixing-length hypothesis is to replace the constant ν_{ML} in (3.14)-(3.15) (which is computed only once, at the beginning of the simulation) with a variable turbulent viscosity (which is recomputed at every time step), such as that proposed in Smagorinsky (1963). This yields a POD closure model in which the viscosity coefficient is increased by

$$\nu_S := 2(C_S \delta)^2 \|\mathbb{D}(\mathbf{u}_r)\|, \quad (3.16)$$

where C_S is the Smagorinsky constant, δ is the lengthscale defined in §3.2 and $\|\mathbb{D}(\mathbf{u}_r)\|$ is the Frobenius norm of the deformation tensor $\mathbb{D}(\mathbf{u}_r)$. Using the EV ansatz in (3.16), the *Smagorinsky POD reduced-order model (S-POD-ROM)* has the form (3.11), where

$$\tilde{b}_k(\mathbf{a}) = -2(C_S \delta)^2 \left(\nabla \varphi_k, \|\mathbb{D}(\mathbf{u}_r)\| \frac{\nabla \mathbf{U} + \nabla \mathbf{U}^T}{2} \right), \quad (3.17)$$

$$\tilde{A}_{km}(\mathbf{a}) = -2(C_S \delta)^2 \left(\nabla \varphi_k, \|\mathbb{D}(\mathbf{u}_r)\| \frac{\nabla \varphi_m + \nabla \varphi_m^T}{2} \right). \quad (3.18)$$

The S-POD-ROM (3.17)-(3.18) was proposed in Borggaard *et al.* (2008) (see also Noack *et al.* 2002) and was used in the reduced-order modeling of structurally dominated 3D turbulent flows in Wang *et al.* (2011); Ullmann & Lang (2010). Its advantage over the ML-POD-ROM (3.14)-(3.15) is obvious: the latter utilizes a constant EV coefficient at every time step, whereas the former recomputes the EV coefficient (which depends on $\|\mathbb{D}(\mathbf{u}_r)\|$) at every time step. To address the significant computational burden posed by the recalculation of the Smagorinsky EV coefficient at every time step, a novel two-level discretization algorithm proposed in Wang *et al.* (2011) is employed in §4.

3.3.3. The Variational Multiscale POD reduced-order model (VMS-POD-ROM)

The VMS method, a state-of-the-art LES closure modeling strategy, was introduced in Hughes *et al.* (2000, 2001a,b). The VMS method is based on the principle of *locality* of energy transfer, i.e., it uses the ansatz that energy is transferred mainly between the neighboring scales. In Couplet *et al.* (2003), the transfer of energy among POD modes for turbulent flow past a backward-facing step (a non-homogeneous separated flow) was investigated numerically. In their report, it was shown that the Fourier-decomposition based concepts of energy cascade and locality of energy transfer are also valid in the POD

context (Figures 3 and 4 in Couplet *et al.* 2003). Thus, VMS closure models represent a natural choice for POD-ROM.

To develop the VMS POD closure model, we start by decomposing the finite set of POD modes \mathbf{X}^r into the direct sum of *large resolved* POD modes \mathbf{X}_L^r and *small resolved* POD modes \mathbf{X}_S^r :

$$\mathbf{X}^r = \mathbf{X}_L^r \oplus \mathbf{X}_S^r, \quad \text{where} \quad (3.19)$$

$$\mathbf{X}_L^r := \text{span} \{ \varphi_1, \varphi_2, \dots, \varphi_{r_L} \} \quad \text{and} \quad (3.20)$$

$$\mathbf{X}_S^r := \text{span} \{ \varphi_{r_L+1}, \varphi_{r_L+2}, \dots, \varphi_r \}. \quad (3.21)$$

Accordingly, we decompose \mathbf{u}_r into two components: \mathbf{u}_r^L representing the *large resolved* scales, and \mathbf{u}_r^S representing the *small resolved* scales:

$$\mathbf{u}_r = \mathbf{u}_r^L + \mathbf{u}_r^S, \quad (3.22)$$

where

$$\mathbf{u}_r^L = \mathbf{U} + \sum_{j=1}^{r_L} a_j \varphi_j, \quad (3.23)$$

$$\mathbf{u}_r^S = \sum_{j=r_L+1}^r a_j \varphi_j. \quad (3.24)$$

The two components \mathbf{u}_r^L and \mathbf{u}_r^S represent the projections of \mathbf{u}_r onto the two spaces \mathbf{X}_L^r and \mathbf{X}_S^r , respectively. The general POD-ROM framework (3.11) can now be separated into two equations - one for \mathbf{a}^L (the vector of POD coefficients of \mathbf{u}_r^L) and one for \mathbf{a}^S (the vector of POD coefficients of \mathbf{u}_r^S). The *Variational Multiscale POD reduced-order model (VMS-POD-ROM)* applies an eddy viscosity term to the small resolved scales only, following the principle of locality of energy transfer. The VMS-POD-ROM reads:

$$\begin{aligned} \begin{bmatrix} \dot{\mathbf{a}}^L \\ \dot{\mathbf{a}}^S \end{bmatrix} &= \begin{bmatrix} \mathbf{b}^L \\ \mathbf{b}^S \end{bmatrix} + \mathbf{A}^r \begin{bmatrix} \mathbf{a}^L \\ \mathbf{a}^S \end{bmatrix} + \begin{bmatrix} \mathbf{A}^L & \mathbf{0} \\ \mathbf{0} & \mathbf{A}^S + \tilde{\mathbf{A}}^S(\mathbf{a}^S) \end{bmatrix} \begin{bmatrix} \mathbf{a}^L \\ \mathbf{a}^S \end{bmatrix} \\ &+ \begin{bmatrix} \mathbf{a}^L \\ \mathbf{a}^S \end{bmatrix}^T \mathbf{B} \begin{bmatrix} \mathbf{a}^L \\ \mathbf{a}^S \end{bmatrix} \end{aligned} \quad (3.25)$$

The finite dimensional system (3.25) can be written componentwise as follows:

$$\dot{a}_k^L(t) = b_k^L + \sum_{m=1}^r A_{km}^r a_m(t) + \sum_{j=1}^{r_L} A_{kj}^L a_j(t) + \sum_{m=1}^r \sum_{n=1}^r B_{kmn} a_n(t) a_m(t), \quad (3.26)$$

$$\forall k = 1, \dots, r_L,$$

$$\begin{aligned} \dot{a}_k^S(t) &= b_k^S + \sum_{m=1}^r A_{km}^r a_m(t) + \sum_{j=r_L+1}^r \left(A_{kj}^S + \tilde{A}_{kj}^S \right) a_j(t) \\ &+ \sum_{m=1}^r \sum_{n=1}^r B_{kmn} a_n(t) a_m(t) \end{aligned} \quad (3.27)$$

$$\forall k = r_L + 1, \dots, r,$$

where

$$b_k^L = -(\varphi_k, \mathbf{U} \cdot \nabla \mathbf{U}) - \frac{2}{\text{Re}} \left(\nabla \varphi_k, \frac{\nabla \mathbf{U} + \nabla \mathbf{U}^T}{2} \right), \quad (3.28)$$

$$A_{km}^r = -(\varphi_k, \mathbf{U} \cdot \nabla \varphi_m) - (\varphi_k, \varphi_m \cdot \nabla \mathbf{U}), \quad (3.29)$$

$$A_{kj}^L = -\frac{2}{\text{Re}} \left(\nabla \varphi_k, \frac{\nabla \varphi_j + \nabla \varphi_j^T}{2} \right), \quad (3.30)$$

$$B_{kmn} = -(\varphi_k, \varphi_m \cdot \nabla \varphi_n), \quad (3.31)$$

$$b_k^S = -(\varphi_k, \mathbf{U} \cdot \nabla \mathbf{U}), \quad (3.32)$$

$$A_{kj}^S = -\frac{2}{\text{Re}} \left(\nabla \varphi_k, \frac{\nabla \varphi_j + \nabla \varphi_j^T}{2} \right), \quad (3.33)$$

$$\tilde{A}_{kj}^S(\mathbf{a}) = -2(C_S \delta)^2 \left(\nabla \varphi_k, \|\mathbb{D}(\mathbf{u}_r^S + \mathbf{U})\| \frac{\nabla \varphi_j + \nabla \varphi_j^T}{2} \right). \quad (3.34)$$

We emphasize that the system of equations (3.25) is *coupled* through two terms: (i) $\mathbf{a}^T \mathbf{B} \mathbf{a}$, which represents the nonlinearity $(\mathbf{u}^r \cdot \nabla) \mathbf{u}^r$; and (ii) $\mathbf{A}^r \mathbf{a}$, which represents the term $(\mathbf{u}^r \cdot \nabla) \mathbf{u}^r$ linearized around the centering trajectory \mathbf{U} . The difference between the VMS-POD-ROM (3.25)-(3.34) and the S-POD-ROM (3.17)-(3.18) is that the former acts only on the small resolved scales (since the Smagorinsky EV term $(C_S \delta)^2 \|\mathbb{D}(\mathbf{u}_r^S + \mathbf{U})\|$ is included only in the equation corresponding to \mathbf{a}^S), whereas the latter acts on all (both large and small) resolved scales.

The VMS-POD-ROM (3.25)-(3.34) was announced in Borggaard *et al.* (2008). This study, however, represents its first careful derivation and through investigation in the numerical simulation of a 3D turbulent flow. We note that a fundamentally different VMS LES closure model that utilizes the NSE residual was proposed in Bazilevs *et al.* (2007); this model was used in a POD setting in Bergmann *et al.* (2009). Yet another VMS-POD-ROM, inspired from the numerical stabilization methods developed in Layton (2002); Guermond (1999); John & Kaya (2005); John & Kindl (2010), was proposed, analyzed and tested in Iliescu & Wang (2010). We emphasize that the VMS-POD-ROM (3.25)-(3.34) is different from both the model used in Bergmann *et al.* (2009) and that used in Iliescu & Wang (2010).

3.3.4. Dynamic Subgrid-Scale POD reduced-order model (DS-POD-ROM)

For all three POD-ROM closure models defined up to this point (i.e., ML-POD-ROM (3.14)-(3.15), S-POD-ROM (3.17)-(3.18), and VMS-POD-ROM (3.25)-(3.34)), the definition has been entirely phenomenological. Indeed, arguing that the role of the discarded POD modes is to extract energy from the system, we used an EV ansatz to derive closure models of increasing complexity and physical accuracy. The *dynamic subgrid-scale (DS)* POD-ROM closure model is also of EV type. Its derivation, however, needs a precise definition of the filtering operation. The DS closure model has its origins in LES, where it is considered state-of-the-art (see for example Sagaut 2006). In LES, the filtering operation is effected by convolving the flow variables with a rapidly decaying spatial filter. In POD, the filtering operation is effected by using the POD Galerkin projection described in §3.1 (see (3.1)). To derive the precise POD filtered equations, we start with the NSE (2.1) in which the velocity \mathbf{u} is replaced by its POD approximation

$\mathbf{u}(\mathbf{x}, t) \approx \mathbf{u}_r(\mathbf{x}, t) \equiv \mathbf{U}(\mathbf{x}) + \sum_{j=1}^r a_j(t) \boldsymbol{\varphi}_j(\mathbf{x})$ in (2.6), and obtain

$$\frac{\partial \mathbf{u}_r}{\partial t} - Re^{-1} \Delta \mathbf{u}_r + (\mathbf{u}_r \cdot \nabla) \mathbf{u}_r + \nabla p = 0. \quad (3.35)$$

Using the fact that $\nabla \cdot \mathbf{u}_r = 0$ in (3.35), we get $(\mathbf{u}_r \cdot \nabla) \mathbf{u}_r = \nabla \cdot (\mathbf{u}_r \mathbf{u}_r)$. Thus, (3.35) can be rewritten as

$$\frac{\partial \mathbf{u}_r}{\partial t} - Re^{-1} \Delta \mathbf{u}_r + \nabla \cdot (\mathbf{u}_r \mathbf{u}_r) + \nabla p = 0. \quad (3.36)$$

Applying the POD filtering operation (3.1) to (3.36), using the fact that the POD Galerkin projection is a linear operator, and *assuming* that differentiation and POD filtering commute, we obtain

$$\frac{\partial \bar{\mathbf{u}}_r}{\partial t} - Re^{-1} \Delta \bar{\mathbf{u}}_r + \nabla \cdot (\overline{\mathbf{u}_r \mathbf{u}_r}) + \nabla \bar{p} = 0. \quad (3.37)$$

We note that, if filtering and differentiation do not commute, one has to estimate the commutation error (see for example Vasilyev & Goldstein 2004; Vasilyev *et al.* 1998; Berselli *et al.* 2006). We also note that, since the POD filtering operation is the Galerkin projection (3.1), $\bar{\mathbf{u}}_r = \mathbf{u}_r$. For consistency with the nonlinear term notation, we still use the $\bar{\mathbf{u}}_r$ notation in what follows.

The POD filtered equation (3.37) can be rewritten as

$$\frac{\partial \bar{\mathbf{u}}_r}{\partial t} - Re^{-1} \Delta \bar{\mathbf{u}}_r + \nabla \cdot (\bar{\mathbf{u}}_r \bar{\mathbf{u}}_r) + \nabla \cdot (\boldsymbol{\tau}_r) + \nabla \bar{p} = 0, \quad (3.38)$$

where

$$\boldsymbol{\tau}_r = \overline{\mathbf{u}_r \mathbf{u}_r} - \bar{\mathbf{u}}_r \bar{\mathbf{u}}_r \quad (3.39)$$

is the POD subfilter-scale stress tensor. Thus, the POD-G-ROM (2.7) amounts to setting $\boldsymbol{\tau}_r = 0$. For turbulent flows, as we have already mentioned, this approximation is flawed. Thus, one needs to address the POD closure problem, i.e., to model the POD subfilter-scale stress tensor $\boldsymbol{\tau}_r$ in terms of POD filtered velocity $\bar{\mathbf{u}}_r$. We note that the POD closure problem is exactly the LES closure problem, in which the spatial filtering is replaced by POD Galerkin projection. For all three POD-ROM closure models defined so far in this section (i.e., ML-POD-ROM (3.14)-(3.15), S-POD-ROM (3.17)-(3.18), and VMS-POD-ROM (3.25)-(3.34)), the closure problem has been addressed by assuming an EV ansatz for $\boldsymbol{\tau}_r$. The DS-POD-ROM employs an EV ansatz as well; specifically, the Smagorinsky model is utilized:

$$\boldsymbol{\tau}_r := (C_S \delta)^2 \|\mathbb{D}(\mathbf{u}_r)\|, \quad (3.40)$$

in which C_S is not a constant (as in the Smagorinsky model), but a function of space and time, i.e., $C_S = C_S(\mathbf{x}, t)$. To compute $C_S(\mathbf{x}, t)$, we follow the LES derivation in Sagaut (2006) and replace the LES spatial filtering with the POD Galerkin projection. Since there are two spatial filters in the LES derivation of the DS model, we define a second POD Galerkin projection (in addition to that defined in (3.1)): For all $\mathbf{u} \in \mathbf{X}$, the second (test) Galerkin projection $\tilde{\mathbf{u}} \in \mathbf{X}^R$ (where $R < r$) is the solution of the following equation:

$$(\mathbf{u} - \tilde{\mathbf{u}}, \boldsymbol{\varphi}) = 0 \quad \forall \boldsymbol{\varphi} \in \mathbf{X}^R. \quad (3.41)$$

Applying the second POD filtering operation (3.41) to (3.37), we obtain:

$$\frac{\partial \tilde{\bar{\mathbf{u}}}_r}{\partial t} - Re^{-1} \Delta \tilde{\bar{\mathbf{u}}}_r + \nabla \cdot (\tilde{\bar{\mathbf{u}}}_r \tilde{\bar{\mathbf{u}}}_r) + \nabla \cdot (\tilde{\mathbf{T}}_r) + \nabla \tilde{\bar{p}} = 0, \quad (3.42)$$

where

$$\mathbf{T}_r = \widetilde{\widetilde{\mathbf{u}_r \mathbf{u}_r}} - \widetilde{\mathbf{u}_r} \widetilde{\mathbf{u}_r} \quad (3.43)$$

is the second POD subfilter-scale stress tensor. We note that the following identity (called the ‘‘Germano identity’’ in LES) holds:

$$\mathbf{T}_r = \widetilde{\widetilde{\mathbf{u}_r \mathbf{u}_r}} - \widetilde{\mathbf{u}_r} \widetilde{\mathbf{u}_r} = \left(\widetilde{\widetilde{\mathbf{u}_r \mathbf{u}_r}} - \widetilde{\mathbf{u}_r} \widetilde{\mathbf{u}_r} \right) + \left(\widetilde{\widetilde{\mathbf{u}_r \mathbf{u}_r}} - \widetilde{\mathbf{u}_r} \widetilde{\mathbf{u}_r} \right) = \mathbf{L}_r + \widetilde{\boldsymbol{\tau}}_r, \quad (3.44)$$

where $\mathbf{L}_r = \widetilde{\widetilde{\mathbf{u}_r \mathbf{u}_r}} - \widetilde{\mathbf{u}_r} \widetilde{\mathbf{u}_r}$ and $\widetilde{\boldsymbol{\tau}}_r = \widetilde{\widetilde{\mathbf{u}_r \mathbf{u}_r}} - \widetilde{\mathbf{u}_r} \widetilde{\mathbf{u}_r}$. We assume the same EV ansatz for the two POD subfilter-scale stress tensors, $\boldsymbol{\tau}_r$ and \mathbf{T}_r :

$$\mathbf{T}_r \approx -2 (C_S \delta)^2 \|\mathbb{D}(\widetilde{\mathbf{u}_r})\| \mathbb{D}(\widetilde{\mathbf{u}_r}) \quad (3.45)$$

$$\boldsymbol{\tau}_r \approx -2 (C_S \delta)^2 \|\mathbb{D}(\widetilde{\mathbf{u}_r})\| \mathbb{D}(\widetilde{\mathbf{u}_r}), \quad (3.46)$$

where $\widetilde{\delta}$ is the filter radius used in the second POD filtering operation (3.41). Assuming that C_S remains constant under the second POD filtering (3.41), we obtain:

$$\widetilde{\boldsymbol{\tau}}_r \approx -2 (C_S \delta)^2 \|\mathbb{D}(\widetilde{\mathbf{u}_r})\| \mathbb{D}(\widetilde{\mathbf{u}_r}) \approx -2 (C_S \delta)^2 \|\mathbb{D}(\widetilde{\mathbf{u}_r})\| \mathbb{D}(\widetilde{\mathbf{u}_r}). \quad (3.47)$$

Plugging (3.45) and (3.47) into (3.44) we obtain:

$$-2 (C_S \delta)^2 \|\mathbb{D}(\widetilde{\mathbf{u}_r})\| \mathbb{D}(\widetilde{\mathbf{u}_r}) = \left(\widetilde{\widetilde{\mathbf{u}_r \mathbf{u}_r}} - \widetilde{\mathbf{u}_r} \widetilde{\mathbf{u}_r} \right) - 2 (C_S \delta)^2 \|\mathbb{D}(\widetilde{\mathbf{u}_r})\| \mathbb{D}(\widetilde{\mathbf{u}_r}). \quad (3.48)$$

We note that C_S is the only unknown in (3.48), all the other terms being computable quantities. Since all the terms in (3.48) are tensors, the unknown C_S cannot satisfy all nine equations. Thus, the following least squares approach is considered instead:

$$\begin{aligned} \min_{C_S} & \left[\left(\widetilde{\widetilde{\mathbf{u}_r \mathbf{u}_r}} - \widetilde{\mathbf{u}_r} \widetilde{\mathbf{u}_r} \right) - 2 (C_S \delta)^2 \|\mathbb{D}(\widetilde{\mathbf{u}_r})\| \mathbb{D}(\widetilde{\mathbf{u}_r}) + 2 (C_S \delta)^2 \|\mathbb{D}(\widetilde{\mathbf{u}_r})\| \mathbb{D}(\widetilde{\mathbf{u}_r}) \right] : \\ & \left[\left(\widetilde{\widetilde{\mathbf{u}_r \mathbf{u}_r}} - \widetilde{\mathbf{u}_r} \widetilde{\mathbf{u}_r} \right) - 2 (C_S \delta)^2 \|\mathbb{D}(\widetilde{\mathbf{u}_r})\| \mathbb{D}(\widetilde{\mathbf{u}_r}) + 2 (C_S \delta)^2 \|\mathbb{D}(\widetilde{\mathbf{u}_r})\| \mathbb{D}(\widetilde{\mathbf{u}_r}) \right] \end{aligned} \quad (3.49)$$

The solution $C_S(\mathbf{x}, t)$ of (3.49) is:

$$\begin{aligned} C_S^2(\mathbf{x}, t) = & \quad (3.50) \\ & \frac{\left[\widetilde{\widetilde{\mathbf{u}_r \mathbf{u}_r}} - \widetilde{\mathbf{u}_r} \widetilde{\mathbf{u}_r} \right] : \left[2 \delta^2 \|\mathbb{D}(\widetilde{\mathbf{u}_r})\| \mathbb{D}(\widetilde{\mathbf{u}_r}) - 2 \delta^2 \|\mathbb{D}(\widetilde{\mathbf{u}_r})\| \mathbb{D}(\widetilde{\mathbf{u}_r}) \right]}{\left[2 \delta^2 \|\mathbb{D}(\widetilde{\mathbf{u}_r})\| \mathbb{D}(\widetilde{\mathbf{u}_r}) - 2 \delta^2 \|\mathbb{D}(\widetilde{\mathbf{u}_r})\| \mathbb{D}(\widetilde{\mathbf{u}_r}) \right] : \left[2 \delta^2 \|\mathbb{D}(\widetilde{\mathbf{u}_r})\| \mathbb{D}(\widetilde{\mathbf{u}_r}) - 2 \delta^2 \|\mathbb{D}(\widetilde{\mathbf{u}_r})\| \mathbb{D}(\widetilde{\mathbf{u}_r}) \right]}. \end{aligned}$$

Since the stress tensors can be computed directly from the resolved field, (3.50) yields a time- and space-dependent formula for $C_S(\mathbf{x}, t)$.

Thus, the DS-POD-ROM increases the viscosity coefficient by

$$\nu_{DS} := 2 (C_S(\mathbf{x}, t) \delta)^2 \|\mathbb{D}(\mathbf{u}_r)\|, \quad (3.51)$$

where $C_S(\mathbf{x}, t)$ is the coefficient in (3.50), δ is the lengthscale defined in § 3.2 and $\|\mathbb{D}(\mathbf{u}_r)\|$ the Frobenius norm of the deformation tensor $\mathbb{D}(\mathbf{u}_r)$. Thus, the *Dynamic Subgrid-Scale POD reduced-order model (DS-POD-ROM)* has the form (3.11), where

$$\widetilde{b}_k(\mathbf{a}) = -2 \delta^2 \left(\nabla \varphi_k, C_S^2(\mathbf{x}, t) \|\mathbb{D}(\mathbf{u}_r)\| \frac{\nabla \mathbf{U} + \nabla \mathbf{U}^T}{2} \right), \quad (3.52)$$

$$\widetilde{A}_{km}(\mathbf{a}) = -2 \delta^2 \left(\nabla \varphi_k, C_S^2(\mathbf{x}, t) \|\mathbb{D}(\mathbf{u}_r)\| \frac{\nabla \varphi_m + \nabla \varphi_m^T}{2} \right). \quad (3.53)$$

Note that ν_{DS} defined in (3.51) can take negative values. This can be interpreted as

backscatter, the inverse transfer of energy from high index POD modes to low index ones. The notion of backscatter, well-established in LES (see for example Sagaut 2006), was also found in a POD setting in the numerical investigation in Couplet *et al.* (2003).

4. Numerical tests

In this section, we use a structurally dominated 3D turbulent flow problem to test the four POD-ROMs described in § 3: (i) the ML-POD-ROM (3.14)-(3.15); (ii) the S-POD-ROM (3.17)-(3.18); (iii) the new VMS-POD-ROM (3.25)-(3.34); and (iv) the new DS-POD-ROM (3.52)-(3.53). We also include results for the POD-G-ROM (2.7) (i.e., a POD-ROM without any closure model). A successful POD closure model should at least perform better than the POD-G-ROM (2.7). Finally, a DNS projection of the evolution of the POD modes served as benchmark for our numerical simulations: The closeness to the DNS data was used as a criterion for the success of the POD closure model. The qualitative behavior of all POD-ROMs is judged according to the following two criteria: (i) the kinetic energy spectrum, which represents the temporal average behavior of the POD-ROMs; and (ii) the time evolution of the POD coefficients, which measures the instantaneous behavior of the POD-ROMs. In § 4.1, details of the numerical methods and parameter choices are given. In § 4.2, numerical results are presented and discussed.

4.1. Numerical Methods and Parameter Choices

We investigate all four POD-ROMs in the numerical simulation of 3D flow past a circular cylinder at $Re = 1,000$. The wake of the flow is fully turbulent. A parallel fluid flow solver is employed on a $144 \times 192 \times 16$ finite volume mesh on the time interval $[0, 300]$ to generate the DNS data. For details on numerical discretization, the reader is referred to Appendix A in Wang *et al.* (2011).

Collecting 1,000 snapshots of the velocity field (u_1, u_2, u_3) over the time interval $[0, 75]$ and applying the method of snapshots developed in Sirovich (1987), we obtain the POD basis $\{\varphi_1, \dots, \varphi_N\}$. These POD modes are then interpolated onto a structured quadratic finite element mesh with nodes coinciding with the nodes used in the original DNS finite volume discretization. The first $r = 6$ POD modes capture 84% the system's kinetic energy. These modes are used in all POD-ROMs that we investigate next. For all the POD-ROMs, the time discretization was effected by using the explicit Euler method with $\Delta t = 7.5 \times 10^{-4}$.

It is important to note that the quadratic nonlinearity in the NSE (2.1) allows for easy precomputation of the vector \mathbf{b} , the matrix \mathbf{A} and the tensor \mathbf{B} in the POD-G-ROM (2.8). For the general nonlinear EV POD closure model (3.11), however, the vector $\tilde{\mathbf{b}}(\mathbf{a})$ and the matrix $\tilde{\mathbf{A}}(\mathbf{a})$ that correspond to the additional closure terms have to be recomputed (reassembled) at each time step. Since the POD basis functions are global, although only a few are used in POD-ROMs ($r \ll N$), reassembling $\tilde{\mathbf{b}}(\mathbf{a})$ and $\tilde{\mathbf{A}}(\mathbf{a})$ at each time step would dramatically increase the CPU time of the corresponding POD-ROM. Thus, the major advantage of POD-ROMs (the dramatic decrease of computational time), would be completely lost.

To ensure a high computational efficiency of the POD-ROMs, we utilize two approaches: (1) Instead of updating the closure terms in the POD-ROMs every time step, we recompute them every 1.5 time units (i.e., every 20,000 time steps). The previous numerical investigations in Wang *et al.* (2011) showed that this approach does not compromise the numerical accuracy of the S-POD-ROM (3.17)-(3.18). (2) We employ the two-level algorithm introduced in Wang *et al.* (2011) to discretize the nonlinear closure

models. Before briefly describing the two-level algorithm, we emphasize that, in order to maintain a fair numerical comparison of the four POD-ROMs, we used both algorithmic choices listed above in *all* four POD-ROMs. Therefore, the success or failure of the POD-ROM can solely be attributed to the closure term, which is the only distinguishing feature among all POD-ROMs, and not to the specific algorithmic choices, which are the same for all POD-ROMs.

The two-level algorithm used in all four POD-ROMs is summarized below.

| | |
|---|--------------------------------|
| <pre style="margin: 0;"> $\ell = 0$; compute $\mathbf{b}, \mathbf{A}, \mathbf{B}$ on the <u>fine</u> mesh ; for $\ell = 0$ to $M - 1$ compute $\tilde{\mathbf{b}}(\mathbf{a}^\ell), \tilde{\mathbf{A}}(\mathbf{a}^\ell)$ on the <u>coarse</u> mesh (4.1) $\mathbf{a}^{\ell+1} := \tilde{F}(\mathbf{a}^\ell)$; endfor</pre> | <p>two-level algorithm</p> |
|---|--------------------------------|

In (4.1), M represents the total number of time steps. The idea in the two-level algorithm is straightforward: Instead of computing the closure terms $\tilde{\mathbf{b}}(\mathbf{a}^\ell), \tilde{\mathbf{A}}(\mathbf{a}^\ell)$ directly on the fine mesh (as done in the standard one-level algorithm), the two-level algorithm discretizes them on a *coarser mesh*. Thus, the two-level algorithm is much more efficient than the standard one-level algorithm. Indeed, in Wang *et al.* (2011) it was shown that the two-level algorithm (4.1) achieves the same level of accuracy as the one-level algorithm while decreasing the computational cost by an order of magnitude. In all four POD-ROMs, we apply the two-level algorithm with a coarsening factor $R_c = 4$ in both radial and azimuthal directions. Thus, the vectors and matrices related to the nonlinear closure terms are computed on a coarse finite element mesh with $37 \times 49 \times 17$ grid points.

In §3.2, we proposed two definitions for the POD lengthscale δ . Since in the finite element discretization that we employ, definition (3.10) is harder to implement than (3.9), we use the latter. Thus, using definition (3.9) with $r = 6$, we obtain $\delta = 0.1179$, which is the POD lengthscale that we will use in all four POD-ROMs. For the DS-POD-ROM (3.52)-(3.53), we need to define the second (test) Galerkin projection (3.41) and the corresponding filter radius $\tilde{\delta}$. Choosing $R = 1$ in (3.41) and using (3.9), we obtain $\tilde{\delta} = 0.1769$.

The constants in EV LES models are determined in a straightforward fashion, utilizing scaling laws satisfied by general 3D turbulent flows (see for example Sagaut 2006). Although the energy cascade concept in a POD context was verified numerically in Couplet *et al.* (2003), there are no general scaling laws available in this setting. Thus, to our knowledge, the correct values for the EV constants α in the ML-POD-ROM (3.14)-(3.15) and C_S in the S-POD-ROM (3.17)-(3.18) and the new VMS-POD-ROM (3.25)-(3.34) are still not known. To determine these EV constants, we run the corresponding POD-ROM on the short time interval $[0, 15]$ with several different values for the EV constants and choose the value that yields the results that are closest to the DNS results. This approach yields the following values for the EV constants: $\alpha = 3 \times 10^{-3}$ for the ML-POD-ROM, $C_S = 0.1426$ for the S-POD-ROM, and $C_S = 0.1897$ for the VMS-POD-ROM. We emphasize that these EV constant values are optimal only on the short time interval tested, and they might actually be non-optimal on the entire time interval $[0, 300]$ on which the POD-ROMs are tested. Thus, this heuristic procedure ensures some fairness in the numerical comparison of the four POD-ROMs.

In the VMS-POD-ROM, only the first POD basis is considered as the large resolved POD mode, that is, $r_L = 1$ in (3.20). In the DS-POD-ROM, since ν_{DS} can be negative, we use a standard “clipping” procedure to ensure the numerical stability of the discretization

(see for example Sagaut 2006). Specifically, we let $C_S(\mathbf{x}, t) = \max\{C_S(\mathbf{x}, t), -0.2\}$. The value -0.2 is determined as follows: We first run the DS-POD-ROM without “clipping” for the time interval $[0, 15]$ and record $C_{S,ave}^-$, the average negative value of $C_S(\mathbf{x}, t)$. We then run on the entire time interval $[0, 300]$ the DS-POD-ROM with a “clipping” value $C_{S,ave}^-/2 = -0.2$. We note that there are alternative procedures to deal with the same issue in LES, such as VDSMwc (Morinishi & Vasilyev 2002). We utilized the standard “clipping” procedure described above as a first step in the numerical investigation of the DS-POD-ROM.

4.2. Numerical results

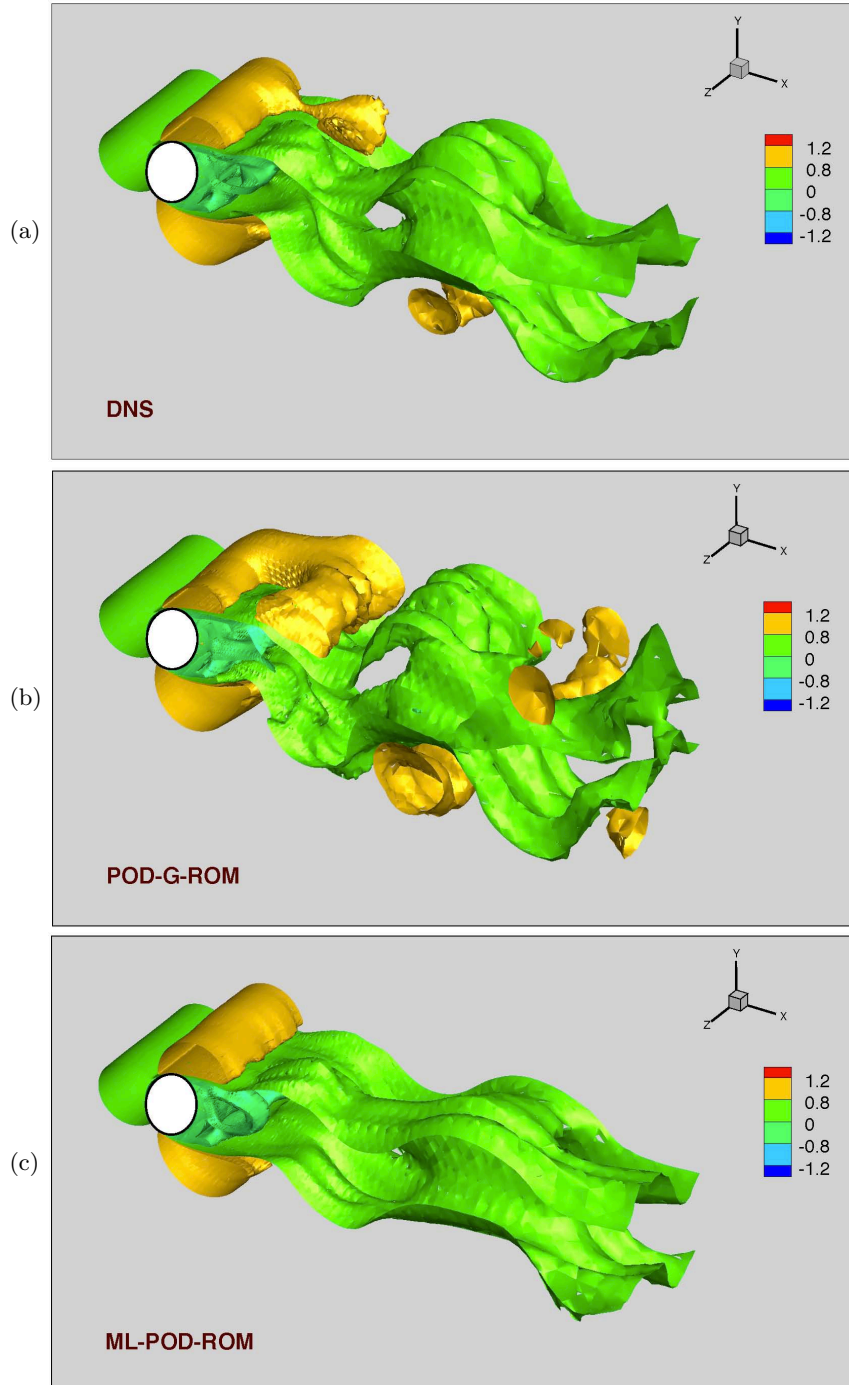
In this section, we test the four POD-ROMs described in §3: (i) the ML-POD-ROM (3.14)-(3.15); (ii) the S-POD-ROM (3.17)-(3.18); (iii) the new VMS-POD-ROM (3.25)-(3.34); and (iv) the new DS-POD-ROM (3.52)-(3.53). To assess their performance, we compare these four POD-ROMs with the POD-G-ROM (2.7) (i.e., POD-ROM without any closure model) and the DNS projection of the evolution of the POD modes. A successful POD-ROM should perform significantly better than the POD-G-ROM and yield results that are close to those from the DNS. The POD-ROM numerical results are judged according to the following two criteria: (i) the kinetic energy spectrum, which represents the temporal average behavior of the POD-ROMs; and (ii) the time evolution of the POD coefficients, which measures the instantaneous behavior of the POD-ROMs. We also include a computational efficiency assessment for all four POD-ROMs.

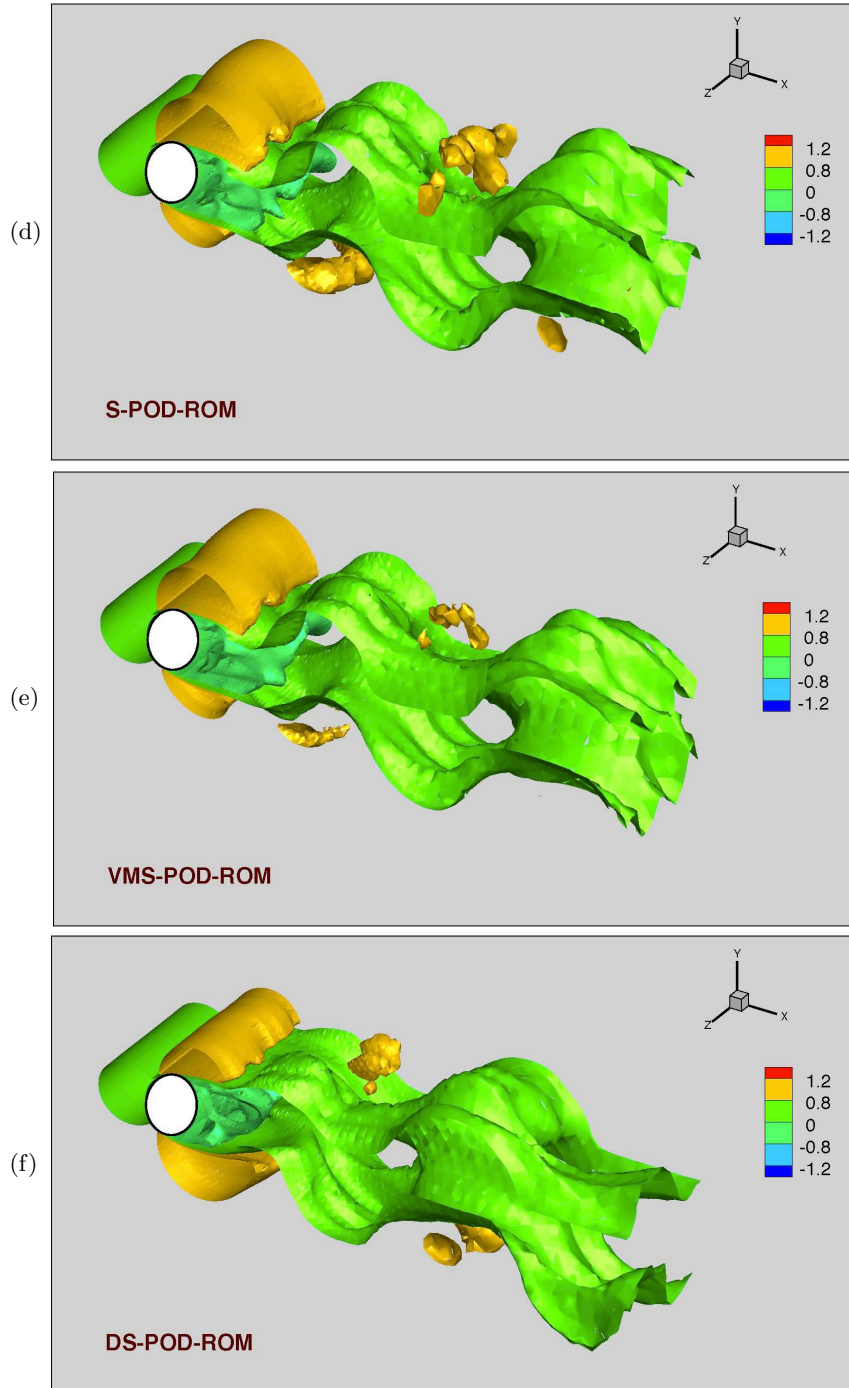
Before starting the quantitative comparison of the four POD-ROMs, we first give a flavor of the topology of the resulting flow fields. Figure 1 presents snapshots of horizontal velocity at $t = 142.4 s$ for DNS, POD-G-ROM, ML-POD-ROM, S-POD-ROM, VMS-POD-ROM, and DS-POD-ROM. For clarity, only five isosurfaces are drawn. Taking the DNS results as a benchmark, the POD-G-ROM seems to add unphysical structures. The ML-POD-ROM, on the other hand, appears to add too much numerical dissipation to the system and thus eliminates some of the vortical structures in the wake. The S-POD-ROM, VMS-POD-ROM, and DS-POD-ROM perform well, capturing a similar amount of structure as the DNS. It also seems that there is some phase shift for all these POD-ROMs. Due to space limitations, only one time instance snapshot is shown for the POD-ROMs. The general behavior over the entire time interval is similar; it can be found at http://www.math.vt.edu/people/wangzhu/POD_3DNumComp.html.

Figure 2 presents the energy spectra of the four POD-ROMs and, for comparison purposes, of the POD-G-ROM. The five energy spectra are compared with the DNS energy spectrum. All energy spectra are calculated from the average kinetic energy of the nodes in the cube with side 0.1 centered at the probe (0.9992, 0.3575, 1.0625). It is clear that the energy spectrum of the POD-G-ROM overestimates the energy spectrum of the DNS. The energy spectrum of the ML-POD-ROM, on the other hand, underestimates the the energy spectrum of the DNS, especially at the higher frequencies. The S-POD-ROM has a more accurate spectrum than the ML-POD-ROM, but it displays high oscillations at the higher frequencies. The VMS-POD-ROM is a clear improvement over the S-POD-ROM, with smaller oscillations at the higher frequencies. The energy spectrum of the DS-POD-ROM is qualitatively similar to that of the VMS-POD-ROM. The DS-POD-ROM spectrum decreases the amplitude of the high frequency oscillations of the VMS-POD-ROM even further, although it introduces some sporadic large amplitude oscillations at high frequencies. To summarize, the DS-POD-ROM and the VMS-POD-ROM yield the most accurate energy spectra, i.e., the closest to the DNS energy spectrum. On the average, the DS-POD-ROM performs slightly better than the VMS-POD-ROM.

As the second criterion in judging the performance of the four POD-ROMs, the time

FIGURE 1. (Continued on next page.) Snapshots of horizontal velocity at $t = 142.5$ s for: (a) DNS; (b) the POD-G-ROM (2.7); (c) the ML-POD-ROM (3.14)-(3.15); (d) the S-POD-ROM (3.17)-(3.18); (e) the new VMS-POD-ROM (3.25)-(3.34); and (f) the new DS-POD-ROM (3.52)-(3.53). Five isosurfaces are plotted. Note that the POD-G-ROM adds unphysical structures, whereas the ML-POD-ROM eliminates some of the DNS structures. The S-POD-ROM, VMS-POD-ROM, and DS-POD-ROM perform well, capturing a similar amount of structure as the DNS.





evolutions of the POD basis coefficients $a_1(\cdot)$ and $a_4(\cdot)$ on the entire time interval $[0, 300]$ are shown in Figures 3-4. We note that the other POD coefficients have a similar behavior. Thus, for clarity of exposition, we include only $a_1(\cdot)$ and $a_4(\cdot)$. The POD-G-ROM's time evolutions of a_1 and a_4 are clearly inaccurate. Indeed, the magnitude of a_4 is nine times larger than that of the DNS projection, which indicates the need for closure modeling. The

ML-POD-ROM's time evolutions of a_1 and a_4 are also inaccurate. Specifically, although the time evolution at the beginning of the simulation (where the EV constant α was chosen) is relatively accurate, the accuracy significantly degrades toward the end of the simulation. For example, the magnitude of a_4 at the end of the simulation is only one eighth of that of the DNS. The S-POD-ROM yields more accurate time evolutions than the ML-POD-ROM for both a_1 and a_4 , although the magnitude of the POD coefficients stays almost constant at a high level. The VMS-POD-ROM's time evolutions of a_1 and a_4 are better than those of the S-POD-ROM, since the magnitudes of the POD coefficients are closer to those of the DNS. Finally, the DS-POD-ROM also yields accurate results. We note that the DS-POD-ROM's a_1 and a_4 coefficients have significantly more variability than the corresponding coefficients of the VMS-POD-ROM. This is a consequence of the fact that the EV coefficient C_S varies in time and space for the DS-POD-ROM, whereas it is constant for the VMS-POD-ROM. To summarize, the DS-POD-ROM and the VMS-POD-ROM perform the best. On the average, the DS-POD-ROM performs slightly better than the VMS-POD-ROM.

Based on the energy spectra and the the time evolutions of the POD basis coefficients $a_1(\cdot)$ and $a_4(\cdot)$, the DS-POD-ROM and the VMS-POD-ROM consistently outperform the ML-POD-ROM and the S-POD-ROM. To determine which one of the DS-POD-ROM and the VMS-POD-ROM performs best, we collected the results in Figures 4(d)–4(e) (corresponding to the time evolution of the POD basis coefficient $a_4(\cdot)$ for the DNS projection, the VMS-POD-ROM and the DS-POD-ROM) and we displayed them in the same plot in Figure 5. Since it is difficult to distinguish between the results from the VMS-POD-ROM and the DS-POD-ROM, we zoomed in on the POD basis coefficient a_4 over the time interval [266, 282]. Based on the plot in the inset, it is clear that, for this time interval, the DS-POD-ROM performs better than the VMS-POD-ROM. More importantly, it appears that the magnitude of a_4 in the DS-POD-ROM displays some of the variability displayed by the DNS; the magnitude of the VMS-POD-ROM's a_4 coefficient, on the other hand, displays an almost periodic behavior. We believe that the variation of the DS-POD-ROM's a_4 coefficient is due to the dynamical computation of the EV coefficient, which changes both in space and time; the EV coefficient of the VMS-POD-ROM, however, is constant and is computed at the beginning of the simulation.

To gain further insight into the behavior of the DS-POD-ROM and the VMS-POD-ROM, we considered the root mean square horizontal velocity of the two models. Figure 6 presents the average horizontal velocity $\langle u \rangle$, which is computed at points with coordinates $x = 3.2937$ and $y = 2.2796$, and the root mean square horizontal velocity $u_{rms} = \langle u - \langle u \rangle, u - \langle u \rangle \rangle^{1/2} / \langle u \rangle$, where $\langle \cdot \rangle$ here denotes the spatial average in the z -direction. Both the DS-POD-ROM and the VMS-POD-ROM yield average horizontal and root mean square velocities that are in close agreement with the DNS data. As for the time evolution of the POD basis coefficient a_4 in Figure 5, the DS-POD-ROM and the VMS-POD-ROM results are practically indistinguishable.

To summarize, the VMS and DS approaches, which are state-of-the-art closure modeling strategies in LES, yield the most accurate POD closure models for the 3D turbulent flow that we investigated. A natural question, however, is whether the new POD closure modeling strategies that we proposed display a high level of computational efficiency, which is one of the trademarks of a successful POD-ROM. To answer this question, we computed the CPU times for all four POD-ROMs and compared them with those of the DNS and the POD-G-ROM.

To make such a comparison, however, we first need to address the numerical differences between the DNS and the POD-ROMs. First, the discretizations used in the two

TABLE 1. Speed-up factors of POD-ROMs.

| | POD-G-ROM | ML-POD-ROM | S-POD-ROM | VMS-POD-ROM | DS-POD-ROM |
|-------|-----------|------------|-----------|-------------|------------|
| S_f | 665 | 659 | 36 | 41 | 23 |

approaches are completely different. Indeed, the spatial discretization used in the DNS was the finite volume method, whereas for the POD-ROMs we used a finite element method. Furthermore, the time-discretization used in the DNS was second-order (Crank-Nicolson and Adams-Bashforth), whereas in the POD-ROMs we used a first-order time discretization (explicit Euler). The time steps employed were also different: $\Delta t = 2 \times 10^{-3}$ in the DNS and $\Delta t = 7.5 \times 10^{-4}$ in the POD-ROM. Most importantly, the DNS was performed on a parallel machine (on 16 processors), whereas all the POD-ROM runs were carried out on a single-processor machine. Thus, to ensure a more realistic comparison between the CPU times of the DNS and the POD-ROMs, we multiplied the CPU time of the DNS by a factor of 16.

To measure the computational efficiency of the four POD-ROMs, we define the speed-up factor

$$S_f = \frac{\text{CPU time of DNS}}{\text{CPU time of POD-ROM}} \quad (4.2)$$

and list results in Table 1. The most efficient model is the POD-G-ROM. This is not surprising, since no closure model is used in POD-G-ROM and thus no CPU time is spent computing an additional nonlinear term at each time step. The second most efficient model is the ML-POD-ROM. This is again natural, since only a linear closure model is employed in the ML-POD-ROM and thus the computational overhead is minimal. The speed-up factors for the S-POD-ROM, the VMS-POD-ROM and the DS-POD-ROM are one order of magnitude lower than those for the ML-POD-ROM and the POD-G-ROM. The reason is that the former use nonlinear closure models, which increase significantly the computational time. Note, however, that the S-POD-ROM, the VMS-POD-ROM and the DS-POD-ROM are still significantly more efficient than the DNS.

FIGURE 2. Kinetic energy spectrum of the DNS (blue) and the POD-ROMs (red): (a) the POD-G-ROM (2.7) overestimates the DNS spectrum; (b) the ML-POD-ROM (3.14)-(3.15) underestimates the DNS spectrum; (c) the S-POD-ROM (3.17)-(3.18) yields a more accurate spectrum than the ML-POD-ROM, but displays high oscillations at the higher frequencies; (d) the new VMS-POD-ROM (3.25)-(3.34) clearly improves the accuracy of the S-POD-ROM's spectrum, displaying smaller oscillations at the higher frequencies; and (e) the new DS-POD-ROM (3.52)-(3.53) decreases the amplitude of the high oscillations of the VMS-POD-ROM's spectrum, although it displays sporadic undershoots.

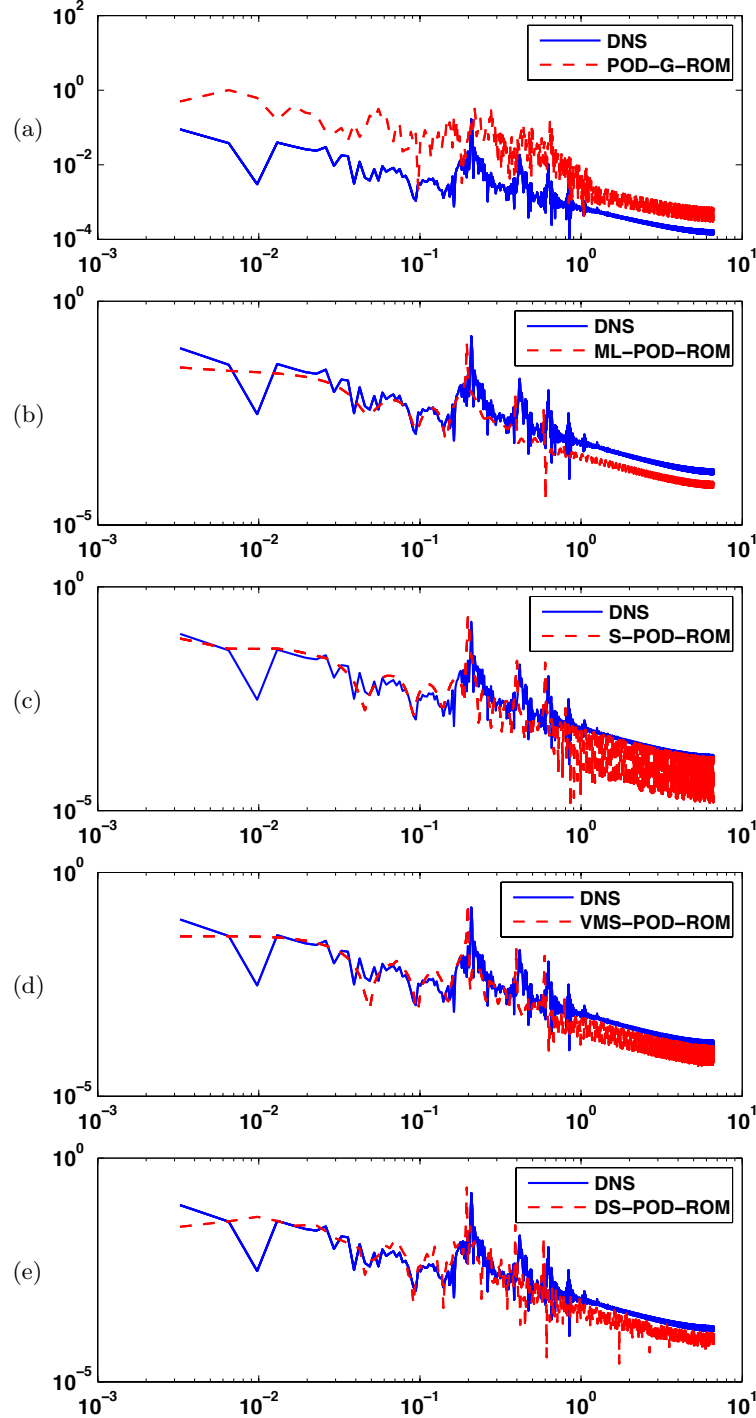


FIGURE 3. Time evolutions of the POD basis coefficient a_1 of the DNS (blue) and the POD-ROMs (red): (a) the POD-G-ROM (2.7) overestimates the DNS results; (b) the ML-POD-ROM (3.14)-(3.15) underestimates the DNS results; (c) the S-POD-ROM (3.17)-(3.18) yields more accurate results than the ML-POD-ROM; (d) the new VMS-POD-ROM (3.25)-(3.34) improves the accuracy of the S-POD-ROM results, especially toward the end of the simulation; and (e) the new DS-POD-ROM (3.52)-(3.53) yields results that are similar to those of the VMS-POD-ROM.

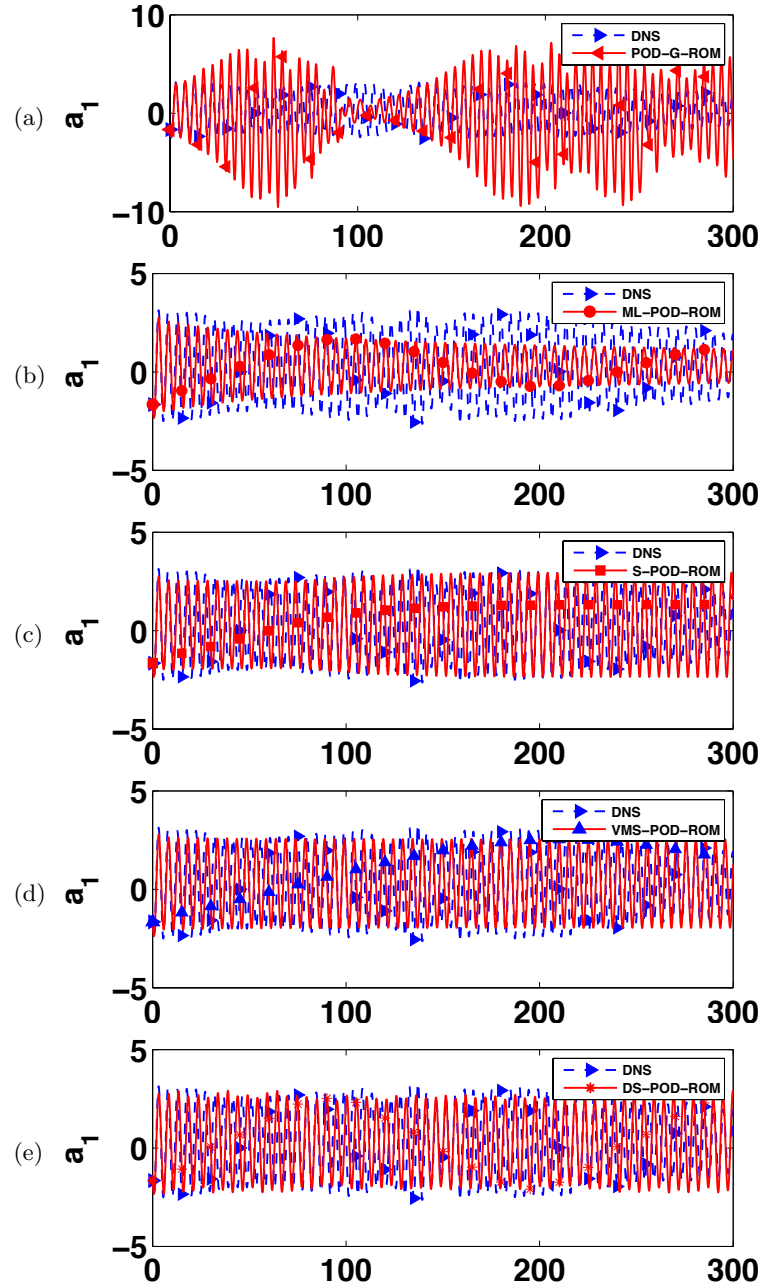


FIGURE 4. Time evolutions of the POD basis coefficient a_4 of the DNS (blue) and the POD-ROMs (red): (a) the POD-G-ROM (2.7) overestimates the DNS results; (b) the ML-POD-ROM (3.14)-(3.15) underestimates the DNS results; (c) the S-POD-ROM (3.17)-(3.18) yields more accurate results than the ML-POD-ROM; (d) the new VMS-POD-ROM (3.25)-(3.34) improves the accuracy of the S-POD-ROM results, especially toward the end of the simulation; and (e) the new DS-POD-ROM (3.52)-(3.53) performs slightly better than the VMS-POD-ROM, recovering some of the variability of the DNS results.

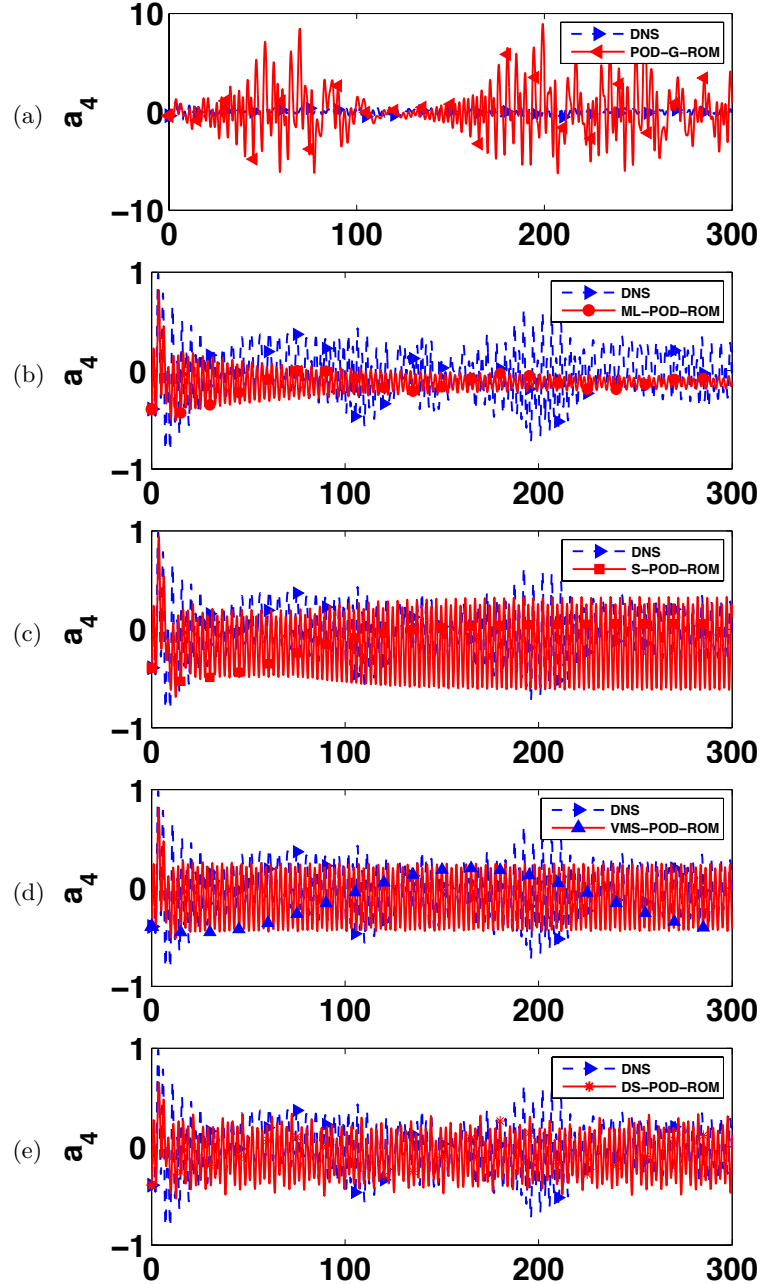


FIGURE 5. Time evolutions of the POD basis coefficient a_4 of the DNS (green), the new VMS-POD-ROM (3.25)-(3.34) (blue), and the new DS-POD-ROM (3.52)-(3.53) (red). The inset shows that the DS-POD-ROM performs better than the VMS-POD-ROM, capturing some of the variability displayed by the DNS results.

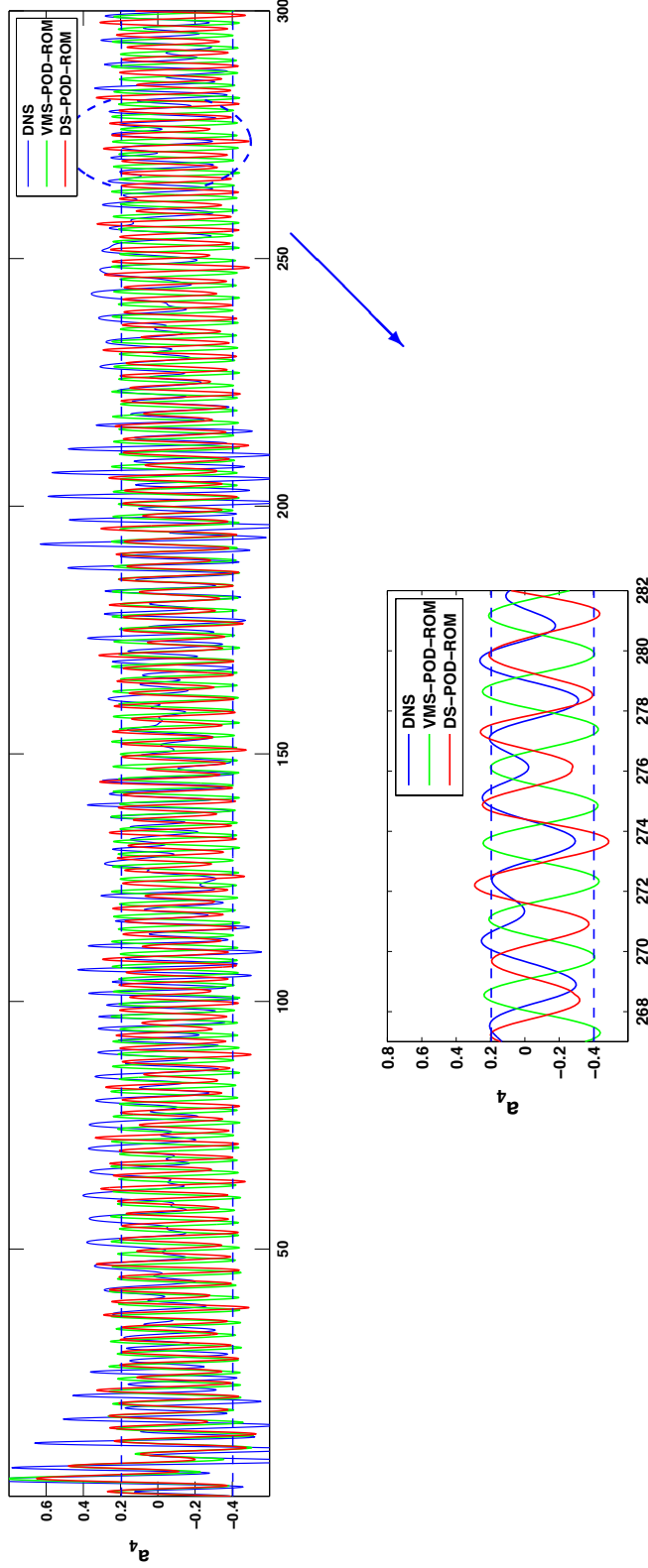
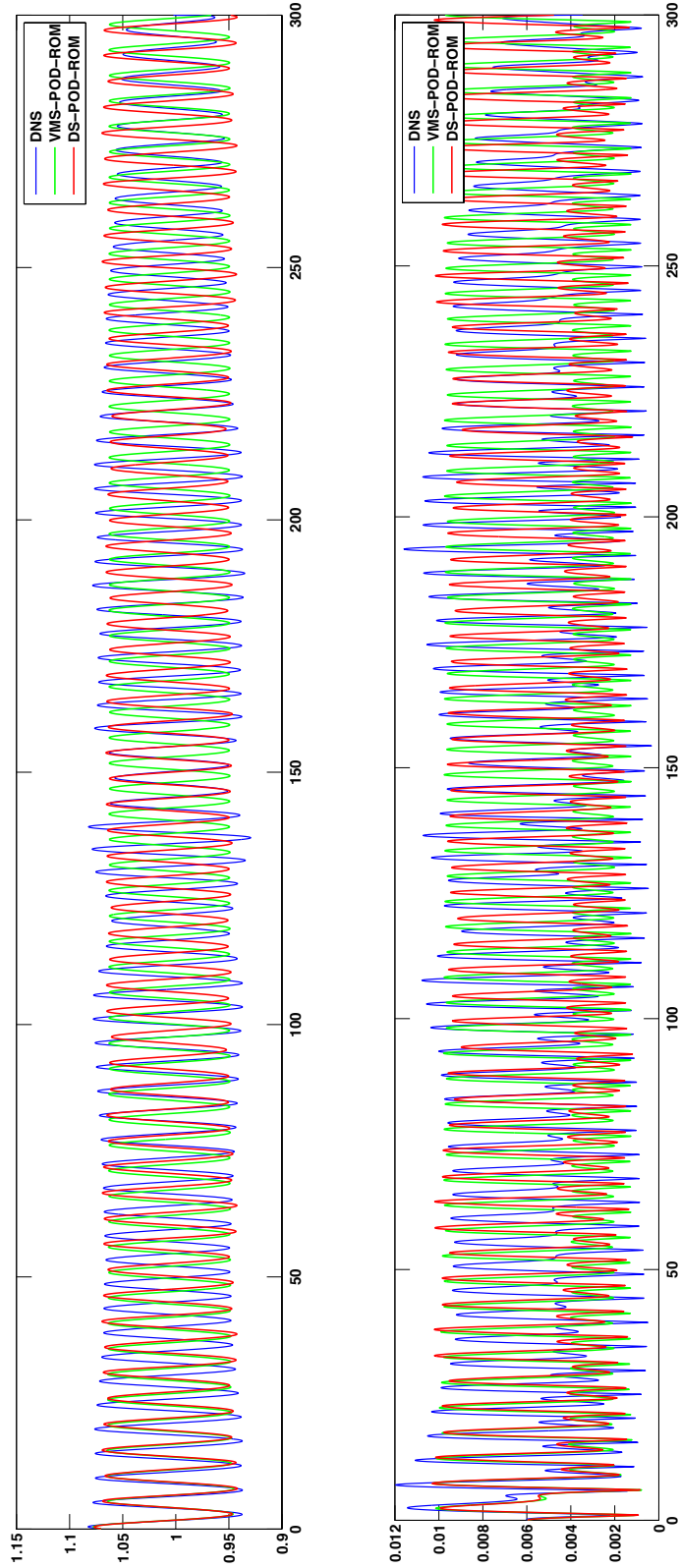


FIGURE 6. Time evolutions of the average horizontal velocity (top) and the root mean square horizontal velocity (bottom) of the DNS (green), the new VMS-POD-ROM (3.25)-(3.34) (blue), and the new DS-POD-ROM (3.52)-(3.53) (red). The DS-POD-ROM and the VMS-POD-ROM yield similar results.



5. Conclusions

This paper put forth two new POD-ROMs (the DS-POD-ROM and the VMS-POD-ROM), which are inspired from state-of-the-art LES closure modeling strategies. These two new POD-ROMs together with the ML-POD-ROM and the S-POD-ROM were tested in the numerical simulation of a 3D turbulent flow past a cylinder at $Re = 1,000$. For completeness, we also included results with the POD-G-ROM (i.e., a POD-ROM without any closure model), as well as the DNS projection of the evolution of the POD modes, which served as benchmark for our numerical simulations.

To assess the performance of the POD-ROMs, two criteria were considered in this paper: the kinetic energy spectrum and the time evolution of the POD basis coefficients. The former is used to measure the average behavior of the POD-ROMs and the latter is used to quantify the instantaneous behavior of these models. Both the POD-G-ROM and the ML-POD-ROM yielded inaccurate results. The DS-POD-ROM and the VMS-POD-ROM clearly outperformed these two models, yielding more accurate results for both the kinetic energy spectrum and the time evolution of the POD basis coefficients. The DS-POD-ROM performed slightly better than the VMS-POD-ROM for both criteria and also seemed to display more adaptivity in terms of adjusting the magnitude of the POD basis coefficients. Overall, however, the two models yielded similar qualitative results. This seems to reflect the LES setting, where both the DS and the VMS closure modeling strategies are considered state-of-the-art (Hughes *et al.* 2001*a,b*). The DS-POD-ROM and the VMS-POD-ROM, although not as computationally efficient as the POD-G-ROM or the ML-POD-ROM, significantly decreased the CPU time of the DNS. To summarize, for the 3D turbulent flow that we investigated, the DS-POD-ROM and the VMS-POD-ROM were found to perform the best among the POD-ROMs investigated, combining a relative high numerical accuracy with a high level of computational efficiency.

We plan to further investigate several other research avenues. First, we plan to study more efficient time-discretization approaches and take advantage of parallel computing in order to further decrease the computational time and, at the same time, increase the dimension (and the thus physical accuracy) of the POD-ROMs. Second, since the linear closure model (ML-POD-ROM) is computationally efficient, but only works on a relative short time interval if the appropriate EV coefficient α is chosen, we will investigate a hybrid approach: We will use the DS approach to calculate α only when the flow displays a high level of variability, and then use this value in the ML-POD-ROM as long as the flow does not experience sudden transitions. Third, using these computational developments, we will investigate the new POD-ROMs in more challenging, higher Reynolds number structurally dominated turbulent flows. Finally, we plan to employ the new POD-ROMs in other scientific and engineering applications in which accurate POD closure modeling is needed, such as optimal control, optimization, and data assimilation problems.

We greatly appreciate the financial support of the Air Force Office of Scientific Research through grant FA9550-08-1-0136 and of the National Science Foundation through grant DMS-1016450. A significant part of the computations were carried out on SystemX at Virginia Tech's Advanced Research Computing center (<http://www.arc.vt.edu>). The allocation grant and support provided by the staff are gratefully acknowledged.

REFERENCES

- AHUJA, S. & ROWLEY, C. W. 2010 Feedback control of unstable steady states of flow past a flat plate using reduced-order estimators. *J. Fluid Mech.* **645**, 447–478.
- AKHTAR, I. & NAYFEH, A. H. 2010 Model based control of laminar wake using fluidic actuation. *J. Comput. Nonlinear Dyn.* **5**, 041015.
- AKHTAR, I., NAYFEH, A. H. & RIBBENS, C. J. 2009 On the stability and extension of reduced-order Galerkin models in incompressible flows. *Theor. Comp. Fluid Dyn.* **23** (3), 213–237.
- AUBRY, N., HOLMES, P., LUMLEY, J. L. & STONE, E. 1988 The dynamics of coherent structures in the wall region of a turbulent boundary layer. *J. Fluid Mech.* **192**, 115–173.
- BAGHERI, S., BRANDT, L. & HENNINGSON, D. 2009 Input–output analysis, model reduction and control of the flat-plate boundary layer. *J. Fluid Mech.* **620**, 263–298.
- BARBAGALLO, A., SIPP, D. & SCHMID, P. 2009 Closed-loop control of an open cavity flow using reduced-order models. *J. Fluid Mech.* **641**, 1–50.
- BARRAULT, M., MADAY, Y., NGUYEN, N. C. & PATERA, A. T. 2004 An ‘empirical interpolation’ method: Application to efficient reduced-basis discretization of partial differential equations. *C. R. Acad. Sci. Paris, Ser. I* **339**, 667–672.
- BAZILEVS, Y., CALO, V. M., COTTRELL, J. A., HUGHES, T. J. R., REALI, A. & SCOVAZZI, G. 2007 Variational multiscale residual-based turbulence modeling for large eddy simulation of incompressible flows. *Comput. Methods Appl. Mech. Engrg.* **197** (1-4), 173–201.
- BERGMANN, M., BRUNEAU, C. H. & IOLLO, A. 2009 Enablers for robust POD models. *J. Comput. Phys.* **228** (2), 516–538.
- BERGMANN, M., CORDIER, L. & BRANCHER, J. 2005 Optimal rotary control of the cylinder wake using proper orthogonal decomposition reduced-order model. *Phys. Fluids* **17**, 097101.
- BERSELLI, L. C., ILIESCU, T. & LAYTON, W. J. 2006 *Mathematics of large eddy simulation of turbulent flows*. Springer-Verlag, Berlin.
- BORGGAARD, J., DUGGLEBY, A., HAY, A., ILIESCU, T. & WANG, Z. 2008 Reduced-order modeling of turbulent flows. In *Proceedings of MTNS 2008*.
- BUFFONI, M., CAMARRI, S., IOLLO, A. & SALVETTI, M. V. 2006 Low-dimensional modelling of a confined three-dimensional wake flow. *J. Fluid Mech.* **569**, 141–150.
- CAZEMIER, W., VERSTAPPEN, R. & VELDMAN, A. 1998 Proper orthogonal decomposition and low-dimensional models for driven cavity flows. *Phys. Fluids* **10**, 1685.
- CHATURANTABUT, S., SORENSEN, D. C. & STEVEN, J. C. 2010 Nonlinear model reduction via discrete empirical interpolation. *SIAM J. Sci. Comput.* **32** (5), 2737–2764.
- COHEN, K., SIEGEL, S., MCLAUGHLIN, T. & GILLIES, E. 2003 Feedback control of a cylinder wake low-dimensional model. *AIAA J.* **41** (7), 1389–1391.
- COUPLET, M., SAGAUT, P. & BASDEVANT, C. 2003 Intermodal energy transfers in a proper orthogonal decomposition–Galerkin representation of a turbulent separated flow. *J. Fluid Mech.* **491**, 275–284.
- DAESCU, D. & NAVON, I. 2008 A dual-weighted approach to order reduction in 4DVAR data assimilation. *Mon. Weather Rev.* **136** (3), 1026–1041.
- DICKINSON, B. T. & SINGLER, J. R. 2010 Nonlinear model reduction using group proper orthogonal decomposition. *Int. J. Numer. Anal. Mod.* **7** (2), 356–372.
- FANG, F., PAIN, C., NAVON, I., PIGGOTT, M., GORMAN, G., FARRELL, P., ALLISON, P. & GODDARD, A. 2009 A POD reduced-order 4D-Var adaptive mesh ocean modelling approach. *Internat. J. Numer. Methods Fluids* **60** (7), 709–732.
- GALBALLY, D., FIDKOWSKI, K., WILLCOX, K. & GHATTAS, O. 2010 Non-linear model reduction for uncertainty quantification in large-scale inverse problems. *Int. J. Numer. Meth. Eng.* **81** (12), 1581–1608.
- GERMANO, M., PIOMELLI, U., MOIN, P. & CABOT, W. 1991 A dynamic subgrid-scale eddy viscosity model. *Phys. Fluids A* **3**, 1760–1765.
- GRAHAM, W. R., PERAIRE, J. & TANG, K. Y. 1999 Optimal control of vortex shedding using low-order models. part II – model-based control. *Int. J. Numer. Meth. Eng.* **44**, 973–990.
- GUERMOND, J.-L. 1999 Stabilization of Galerkin approximations of transport equations by subgrid modeling. *M2AN Math. Model. Numer. Anal.* **33** (6), 1293–1316.
- HAY, A., BORGGAARD, J., AKHTAR, I. & PELLETIER, D. 2010 Reduced-order models for parameter dependent geometries based on shape sensitivity analysis. *J. Comput. Phys.* **229** (4), 1327–1352.

- HAY, A., BORGGAAARD, J. & PELLETIER, D. 2009 Local improvements to reduced-order models using sensitivity analysis of the proper orthogonal decomposition. *J. Fluid Mech.* **629**, 41–72.
- HOEPFFNER, J., AKERVIK, E., EHRENSTEIN, U. & HENNINGSON, D. S. 2006 Control of cavity-driven separated boundary layer. In *Proc. Conference on Active Flow Control*. Berlin.
- HOLMES, P., LUMLEY, J. L. & BERKOOZ, G. 1996 *Turbulence, Coherent Structures, Dynamical Systems and Symmetry*. Cambridge.
- HUGHES, T. J. R., MAZZEI, L. & JANSEN, K. E. 2000 Large eddy simulation and the variational multiscale method. *Comput. Vis. Sci.* **3**, 47–59.
- HUGHES, T. J. R., MAZZEI, L., OBERAI, A. & WRAY, A. 2001a The multiscale formulation of large eddy simulation: Decay of homogeneous isotropic turbulence. *Phys. Fluids* **13** (2), 505–512.
- HUGHES, T. J. R., OBERAI, A. & MAZZEI, L. 2001b Large eddy simulation of turbulent channel flows by the variational multiscale method. *Phys. Fluids* **13** (6), 1784–1799.
- ILIESCU, T. & WANG, Z. 2010 Variational multiscale proper orthogonal decomposition: Convection dominated convection-diffusion equations Submitted.
- ITO, K. & RAVINDRAN, S. S. 1998 A reduced-order method for simulation and control of fluid flows. *J. Comput. Phys.* **143** (2), 403–425.
- JOHN, V. & KAYA, S. 2005 A finite element variational multiscale method for the Navier–Stokes equations. *SIAM J. Sci. Comput.* **26**, 1485.
- JOHN, V. & KINDL, A. 2010 A variational multiscale method for turbulent flow simulation with adaptive large scale space. *J. Comput. Phys.* **229**, 301–312.
- LAYTON, W. J. 2002 A connection between subgrid scale eddy viscosity and mixed methods. *Appl. Math. Comput.* **133**, 147–157.
- LEHMANN, O., LUCHTENBURG, M., NOACK, B. R., KING, R., MORZYŃSKI, M. & TADMOR, G. 2005 Wake stabilization using POD Galerkin models with interpolated modes. In *Proc. 44th IEEE Conference on Decision and Control*.
- LUO, Z., ZHU, J., WANG, R. & NAVON, I. M. 2007 Proper orthogonal decomposition approach and error estimation of mixed finite element methods for the tropical Pacific Ocean reduced gravity model. *Comput. Methods Appl. Mech. Engrg.* **196** (41–44), 4184–4195.
- MA, X. & KARNIADAKIS, G. E. 2002 A low-dimensional model for simulating three-dimensional cylinder flow. *J. Fluid Mech.* **458**, 181–190.
- MENEVEAU, C., LUND, T. & CABOT, W. 1996 A Lagrangian dynamic subgrid-scale model of turbulence. *J. Fluid Mech.* **319**, 353–385.
- MORINISHI, Y. & VASILYEV, O. 2002 Vector level identity for dynamic subgrid scale modeling in large eddy simulation. *Phys. Fluids* **14**, 3616.
- NOACK, B., PAPAS, P. & MONKEWITZ, P. 2005 The need for a pressure-term representation in empirical Galerkin models of incompressible shear flows. *J. Fluid Mech.* **523**, 339–365.
- NOACK, B., SCHLEGEL, M., AHLBORN, B., MUTSCHKE, G., MORZYNSKI, M., COMTE, P. & TADMOR, G. 2008 A finite-time thermodynamics of unsteady fluid flows. *J. Non-Equil. Thermody.* **33** (2), 103–148.
- NOACK, B. R., AFANASIEV, K., MORZYNSKI, M., TADMOR, G. & THIELE, F. 2003 A hierarchy of low-dimensional models for the transient and post-transient cylinder wake. *J. Fluid Mech.* **497**, 335–363.
- NOACK, B. R., PAPAS, P. & MONKEWITZ, P. A. 2002 Low-dimensional Galerkin model of a laminar shear-layer. *Tech. Rep.* 2002-01. École Polytechnique Fédérale de Lausanne.
- PODVIN, B. 2001 On the adequacy of the ten-dimensional model for the wall layer. *Phys. Fluids* **13** (1), 210–224.
- PODVIN, B. 2009 A proper-orthogonal-decomposition-based model for the wall layer of a turbulent channel flow. *Phys. Fluids* **21**, 015111.
- PODVIN, B. & LUMLEY, J. 1998 A low-dimensional approach for the minimal flow unit. *J. Fluid Mech.* **362**, 121–155.
- PORTÉ-AGEL, F., MENEVEAU, C. & PARLANGE, M. B. 2000 A scale-dependent dynamic model for large-eddy simulation: application to a neutral atmospheric boundary layer. *J. Fluid Mech.* **415**, 261–284.
- REMPFER, D. 1996 Investigations of boundary layer transition via Galerkin projections on empirical eigenfunctions. *Phys. Fluids* **8**, 175.

- REMPFER, D. & FASEL, H. F. 1994 Dynamics of three-dimensional coherent structures in a flat-plate boundary layer. *J. Fluid Mech.* **275**, 257–283.
- SAGAUT, P. 2006 *Large eddy simulation for incompressible flows*, 3rd edn. Springer-Verlag, Berlin.
- SIRISUP, S. & KARNIADAKIS, G. E. 2004 A spectral viscosity method for correcting the long-term behavior of POD models. *J. Comput. Phys.* **194** (1), 92–116.
- SIROVICH, L. 1987 Turbulence and the dynamics of coherent structures. Parts I–III. *Quart. Appl. Math.* **45** (3), 561–590.
- SMAGORINSKY, J. S. 1963 General circulation experiments with the primitive equations. *Mon. Weather Rev.* **91**, 99–164.
- ULLMANN, S. & LANG, J. 2010 A POD-Galerkin reduced model with updated coefficients for Smagorinsky LES. In *V European Conference on Computational Fluid Dynamics, ECCO-MAS CFD 2010* (ed. J. C. F. Pereira & A. Sequeira). Lisbon, Portugal.
- VASILYEV, O. & GOLDSTEIN, D. 2004 Local spectrum of commutation error in large eddy simulation. *Phys. Fluids* **16** (2), 470–473.
- VASILYEV, O., LUND, T. & MOIN, P. 1998 A general class of commutative filters for LES in complex geometries. *J. Comput. Phys.* **146** (1), 82–104.
- WANG, Z., AKHTAR, I., BORGGAARD, J. & ILIESCU, T. 2011 Two-level discretizations of non-linear closure models for proper orthogonal decomposition. *J. Comput. Phys.* **230**, 126–146.